



Assessing the Photocatalytic Performance of Hydrothermally Synthesized Fe-Doped BiVO₄ Under Low-Intensity UV Irradiation

Melissa Alexander Maran¹ · Alvin Lim Teik Zheng^{1,2} · Hui Yan Tan³ · Shahrul Razid Sarbini³ · Kar Ban Tan⁴ · Supakorn Boonyuen⁵ · Kelly Kai Seng Wong⁶ · Eric Lim Teik Chung^{7,8} · Jacqueline Lease⁹ · Yoshito Andou^{9,10}

Received: 31 December 2024 / Accepted: 24 April 2025
© The Author(s) 2025

Abstract

This study demonstrates the potential of Fe-doped BiVO₄ as an efficient photocatalyst for the degradation of tetracycline (TC). The Fe-doped BiVO₄ was synthesized using the hydrothermal method, resulting in a monoclinic heterostructure with a crystallite size ranging from 27.37 to 29.10 nm and an optical band gap of 2.69–2.87 eV. Photocatalytic tests revealed that 3 wt% Fe doping exhibited the highest degradation efficiency, removing 73.37% of TC in 120 min under a low-power (13 W) UV lamp. The enhanced photocatalytic performance was attributed to the improved electron–hole separation and optimized Fe doping concentration, which facilitated more efficient light absorption and charge carrier dynamics. Additionally, antibacterial tests confirmed the catalyst's ability to inactivate *Staphylococcus aureus*, even in the absence of light, demonstrating its dual functionality in both pollutant degradation and bacterial inactivation. The cost analysis revealed that the synthesized Fe-doped BiVO₄ costs RM 8.17 per gram, further enhancing its appeal for scalable and cost-effective applications. These findings highlight the versatility of Fe-doped BiVO₄ as a photocatalyst for addressing antibiotic-based pollution and waterborne pathogens, making it a promising candidate for practical applications in wastewater treatment and environmental remediation. These findings contribute to global efforts in mitigating waterborne antibiotic and microbial pollution, particularly in regions where access to high-energy treatment technologies is limited.

Keywords Hydrothermal · Photocatalysis · Antibacterial · Fe doping · Water treatment · Environmental remediation

1 Introduction

The degradation of water resources due to human activities and climate change poses a critical threat to sustainable development, recognized as a major global concern by various international organizations. Water sources are contaminated by chemicals and microbes from diverse origins, disrupting ecosystems and limiting water usability [1–4]. Significant contributors to this crisis include household chemicals, industrial effluents, agricultural runoff, and a range of emerging contaminants (ECs). ECs such as pesticides, personal care products, endocrine disruptors, and antibiotics are commonly present in wastewater, groundwater, and surface waters at concentrations higher than anticipated, posing ongoing risks to ecosystems and human health [5–7]. Among these ECs, the antibiotic tetracycline (TC) is particularly concerning. Widely used in medical, veterinary, and agricultural sectors

for its affordability and broad-spectrum antibacterial properties, TC contamination in water bodies introduces several risks, including toxicity, endocrine disruption, and the development of antibiotic-resistant bacteria [3, 8, 9]. Addressing antibiotic contamination in water is challenging, and while conventional treatment methods such as ozonation, membrane filtration, adsorption, and ion exchange are widely used, they often fall short in fully removing pollutants like TC [10–12]. Adsorption, for example, is popular for its simplicity and cost-effectiveness but is limited by low efficiency, incomplete removal, and poor mechanical stability [3, 13–15]. These limitations have led researchers to explore advanced oxidation processes (AOPs), including Fenton reactions, electrochemical oxidation, and photocatalysis, as promising alternatives. Among AOPs, photocatalysis offers distinct advantages, such as the rapid, complete degradation of organic pollutants at ambient temperatures, ultimately converting them to non-toxic by-products like water and carbon dioxide [16–20].

Extended author information available on the last page of the article



Bismuth vanadate (BiVO_4) is a promising semiconductor photocatalyst for solar-driven applications, valued for its eco-friendly synthesis, minimal secondary pollution, and ability to degrade pollutants via reactive oxygen species (ROS) generation. However, BiVO_4 's photocatalytic activity is limited by rapid electron–hole recombination and relatively poor adsorption efficiency [21]. To address these challenges, modifications such as ion doping, noble metal incorporation, and heterojunction formation have been investigated to enhance BiVO_4 's performance. Specifically, doping with transition metals has shown potential for improving photocatalytic efficiency by reducing recombination rates and expanding light absorption [22–24]. Doping semiconductors with metal and non-metal ions has proven effective in reducing the recombination rate of photoinduced charge carriers [25]. Previous study has found that the substitution of a fraction of Bi^{3+} ions with Fe^{3+} ions represent an effective strategy to augment the photoexcitation mechanisms and the adsorption characteristics of BiVO_4 , culminating in a significant enhancement in selective partial oxidation of methane [26]. In addition, doping BiVO_4 with iron (Fe) can introduce intermediate energy levels between the conduction band (CB) and valence band (VB), facilitating improved electron capture and electron–hole separation, which enhances photocatalytic performance [27]. Previous studies have shown that Fe-doped BiVO_4 outperforms bare BiVO_4 in photodegrading contaminants like ibuprofen and *E. coli* under visible light. Regmi and colleagues discovered that the incorporation of Fe into BiVO_4 resulted in the emergence of an in-gap state situated between the VB and the CB of BiVO_4 , which markedly enhanced their photocatalytic efficiency [28]. Thus, the primary goal of this work is to synthesize Fe-doped BiVO_4 via hydrothermal method to investigate how varying Fe concentrations impact their structural, morphological, and optical properties. By examining these properties, this work aims to optimize photocatalytic efficiency for TC degradation under low-power UV light, addressing crucial challenges in sustainable environmental applications.

2 Methodology

2.1 Materials

Bismuth (III) nitrate pentahydrate ($\text{Bi}(\text{NO}_3)_3 \cdot 5\text{H}_2\text{O}$) and ammonium metavanadate (NH_4VO_3) were obtained from Chemiz (M) Sdn. Bhd, while iron (II) sulfate heptahydrate ($\text{FeSO}_4 \cdot 7\text{H}_2\text{O}$), with 99% purity, was purchased from Mallinckrodt Baker, Inc (USA). Tetracycline hydrochloride (TC) was obtained from Wako Chemicals, Japan, and the reagents concentrated nitric acid (HNO_3) and sodium hydroxide (NaOH) were from Sigma-Aldrich. All reagents

were of analytical grade and used without further purification.

2.2 Preparation of BiVO_4 and Fe-Doped BiVO_4

BiVO_4 and Fe-doped BiVO_4 were synthesized hydrothermally using a Teflon-lined autoclave as shown in Fig. 1 as previously reported [29]. Solution A was prepared by dissolving 3.3954 g of $\text{Bi}(\text{NO}_3)_3 \cdot 5\text{H}_2\text{O}$ in 30 mL of 1.5 M HNO_3 . Separately, Solution B was made by dissolving 0.8189 g of NH_4VO_3 in 30 mL of 1.5 M NaOH and was then added to Solution A, resulting in an orange precipitate. As for the Fe doping, $\text{Fe}(\text{NO}_3)_3 \cdot 9\text{H}_2\text{O}$ was introduced at varying weight percentages (0.5 wt%, 1.0 wt%, and 3.0 wt%). The mixture was stirred for 1 h and transferred to an autoclave, where it was heated at 180 °C for 15 h. The hydrothermal method is chosen for their ability to prepare crystalline forms of nanostructures [30]. Following the reaction, the precipitate was washed sequentially with deionized water and ethanol and dried at 60 °C for 12 h. Final calcination at 400 °C for 12 h was performed to enhance crystallinity and stability of materials [31]. Similar procedure was adopted for bare BiVO_4 synthesis, excluding the addition of Fe precursor. The choice of Fe doping concentrations (0.5 wt%, 1.0 wt%, and 3.0 wt%) was guided by prior experimental studies and theoretical predictions [32, 33]. Previously, it was indicated that Fe doping up to 3% optimally enhances photocatalytic performance by improving charge separation and light absorption. Beyond this concentration, excess Fe can lead to lattice distortion and the formation of recombination centers, which negatively impact photocatalytic activity [34]. Thus, our selection of 0.5–3.0 wt% Fe doping allows systematic evaluation of performance trends within this optimal window.

2.3 Characterization

XRD measurements were carried out using a Shimadzu XRD-6000 diffractometer. Scanning was conducted in the 2θ range of 10–80° with a step size of 0.02° and a scanning speed of 1°/min. Crystallite sizes were calculated using the Scherrer equation, focusing on shifts in diffraction patterns to observe any phase changes due to Fe incorporation. (Eq. 1):

$$D = k\lambda / \beta \cos \theta \quad (1)$$

where D is the average crystallite thickness perpendicular to the crystal plane direction, $k = 0.89$ is the Scherrer constant of the diffraction peak, $\lambda = 1.54056$ nm is the X-ray wavelength of Cu-K α radiation, θ is the diffraction angle, and β is the half peak width. FTIR was performed on an Agilent Cary 630 FTIR spectrometer with the KBr pellet method. Spectra were recorded over the 400–4000 cm^{-1} range with baseline and atmospheric corrections applied, identifying

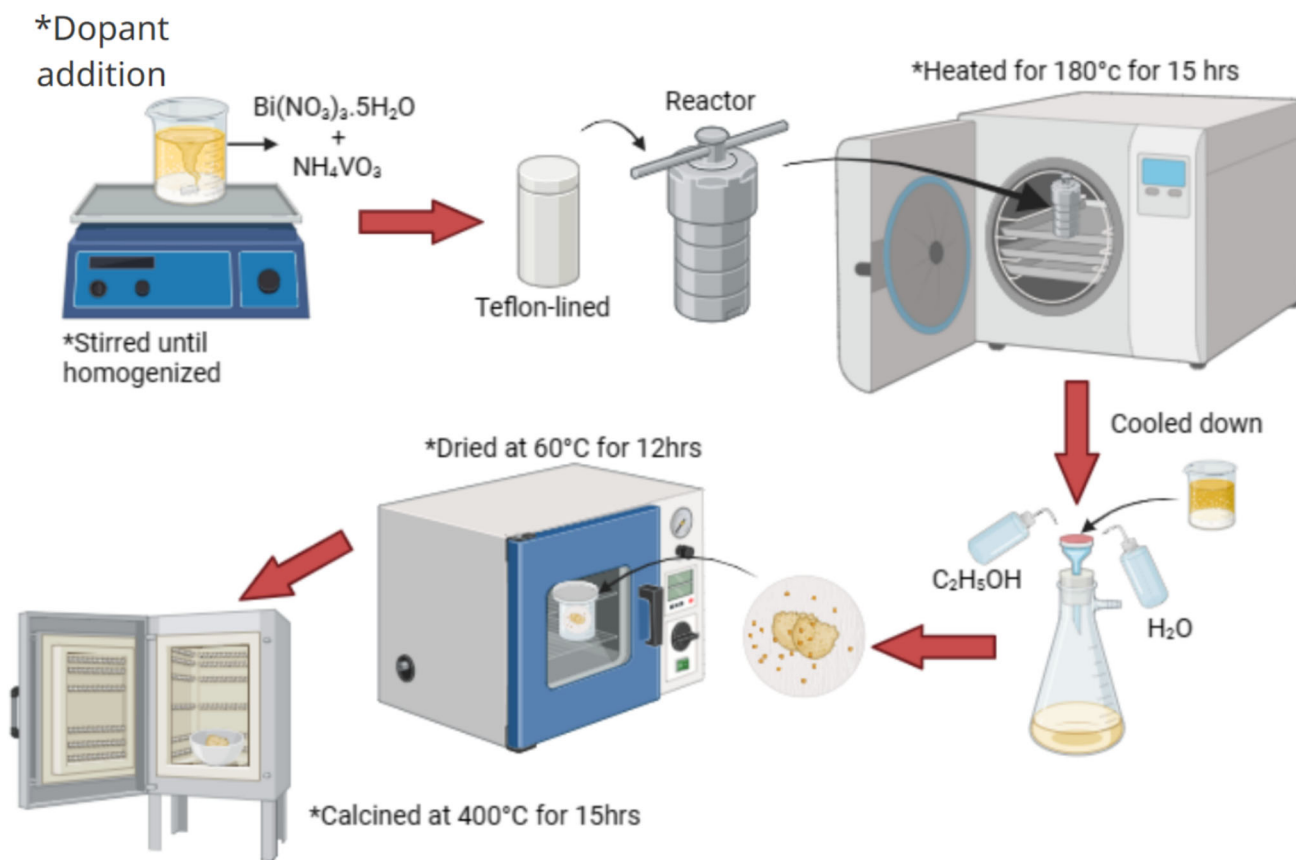


Fig. 1 Flowchart for synthesis of bare and Fe-doped BiVO₄

changes in functional groups due to Fe doping. The morphology of the photocatalysts was accessed on a JCM-6000 Versatile Benchtop Scanning Electron Microscope, JEOL Ltd, Japan. Samples were coated with a thin carbon layer (~ 5 nm) to enhance conductivity. UV–Visible absorption spectra were recorded using IKEMELAB UV1200 UV–Vis spectrophotometer. Absorption edges and bandgap energies were determined by constructing the Tauc plots.

2.4 Photocatalytic Testing

The photocatalytic activity was evaluated using TC degradation under low-intensity UV light irradiation. A 13 W UV aquarium lamp was positioned 10 cm above the reaction vessel to maintain consistent light exposure. Prior to illumination, the catalyst was suspended in the TC solution and stirred in the dark for 30 min to establish adsorption–desorption equilibrium, verified by preliminary trials. For degradation measurements, 10-mL aliquots were sampled every 15 min, centrifuged, and analyzed at 357 nm [35]. The TC degradation efficiency, based on concentration changes, was calculated using a pseudo-first-order (PFO) kinetic model to compare degradation rates across samples [36–40]. The calibration curve for TC is shown in Fig. S1 by

preparing TC aqueous solutions at various concentrations. The photocatalytic degradation efficiency was calculated using the following equation (Eq. 2):

$$\% \text{Degradation} = \frac{C_0 - C_t}{C_0} \times 100\% \quad (2)$$

where C_0 = initial concentration of TC

C_t = concentration of TC after irradiation at ‘t’ minute

2.5 Antibacterial Test

Antibacterial activity was evaluated for the 3% Fe-doped BiVO₄ using the disk diffusion method on both Gram-positive *Staphylococcus aureus* and Gram-negative *Escherichia coli*. Bacterial suspensions with a concentration of 1.5×10^6 CFU/mL (0.5 McFarland standard) were cultured on Mueller–Hinton agar plates. Filter disks impregnated with 1 mg/mL of the catalyst were placed on the agar surface, and plates were incubated at 37 °C in ambient atmospheric conditions. Chloramphenicol and streptomycin served as positive controls, while ethanol was the negative control. The zone of inhibition (ZOI) was measured after 24 h using a vernier caliper. This comparison of ZOI against

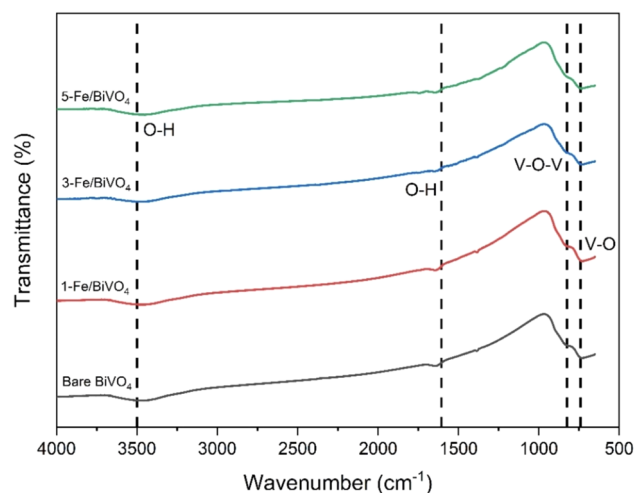


Fig. 2 FTIR spectra of bare and Fe-doped BiVO₄

standard antibiotics and controls allowed for a thorough assessment of the photocatalyst's antibacterial potential. The antibacterial ZOI results are expressed as mean \pm standard deviation (SD) from three independent replicates ($n = 3$) to ensure reproducibility and statistical reliability.

3 Results and Discussion

3.1 Characterization of the Photocatalyst

The FTIR spectra of bare and Fe-doped BiVO₄ were recorded to investigate the surface functional groups and to identify any structural modifications resulting from Fe doping. Figure 2 presents the FTIR spectra, with key peaks corresponding to characteristic functional groups on the catalyst surfaces. The FTIR spectrum exhibits a prominent peak at 3499 cm⁻¹, attributed to the O–H stretching vibrations of adsorbed water molecules on the catalyst surface, while the peak at 1605 cm⁻¹ is associated with the bending vibrations (O–H–O) of physically adsorbed water [41]. These hydroxyl groups are significant for photocatalysis, as they can react with photoexcited holes (h^+) on the BiVO₄ surface to form hydroxyl radicals (\bullet OH), which play a vital role in degrading organic contaminants [42]. The characteristic peak at 832 cm⁻¹ corresponds to V–O–V stretching vibrations in BiVO₄, which confirms the formation of the vanadate structure during synthesis [30]. Additionally, a broad absorption band observed around 742 cm⁻¹ is attributed to the monoclinic BiVO₄'s asymmetric stretching of the V–O bond, indicating the preservation of the monoclinic phase. The Fe doping appears to influence the FTIR spectra subtly, as minor shifts in peak positions and intensity changes are observed in the O–H and V–O–V regions. This shift can be attributed to lattice distortion induced by the Fe ions entering the BiVO₄

matrix, which may impact bond strength and influence the electronic structure of the catalyst. The slight increase in intensity of the O–H bands with Fe doping suggests enhanced surface hydroxylation, which could facilitate more effective ROS formation during photocatalytic reactions, thereby contributing to improved photocatalytic efficiency. It is noted that the FTIR spectra do not display distinct Fe–O stretching bands, likely due to the low doping concentration and the similarity of Fe–O and Bi–O vibrational modes. This absence supports the hypothesis that Fe ions are substitutionally incorporated into the BiVO₄ lattice rather than forming segregated iron oxide phases [43]. The FTIR analysis suggests that Fe doping increases the surface hydroxyl groups, which are essential for photocatalytic degradation of TC due to their role in generating ROS such as \bullet OH. These radicals, along with other reactive species generated during light irradiation, can significantly enhance pollutant degradation. However, FTIR alone cannot unambiguously confirm the oxidation state or lattice position of Fe. To more directly verify Fe incorporation, future studies should employ X-ray photoelectron spectroscopy (XPS) to analyze the chemical state of Fe and electron paramagnetic resonance (EPR) to probe unpaired electrons associated with Fe³⁺. These techniques would validate the electronic role of Fe dopants in enhancing charge carrier separation and photocatalytic activity.

The X-ray diffraction (XRD) patterns of bare and Fe-doped BiVO₄ were obtained to confirm the crystal structure, phase purity, and any structural modifications induced by Fe doping. Figure 3a shows the XRD patterns, while Table 1 summarizes the calculated crystallite sizes, lattice strain, and dislocation density for each sample. The XRD patterns of the bare BiVO₄ display characteristic peaks at 2 θ values of 18.9° (011), 28.9° (121), 30.6° (040), 34.6° (200), and others, which correspond to the monoclinic scheelite structure of BiVO₄ (JCPDS No. 14–0688). This confirms that the synthesized BiVO₄ has the desired monoclinic crystal phase [44, 45]. Notably, no additional peaks are observed after Fe doping, indicating that Fe incorporation did not introduce secondary phases or impurities and that the material maintains its phase purity and structural stability [46]. This stability is advantageous for photocatalytic applications, as it suggests that Fe doping enhances the photocatalyst's properties without compromising its structural integrity. Table 1 shows that Fe doping reduces the crystallite size from 28.8 nm in bare BiVO₄ to 22.3 nm for 3% Fe-doped BiVO₄ and 22.4 nm for 5% Fe-doped BiVO₄. The reduction in crystallite size is beneficial for photocatalytic activity, as smaller crystallites provide a larger surface area, increasing the availability of active sites for photocatalysis [47]. Additionally, reduced crystallite size may promote effective charge separation, as smaller particles typically exhibit lower recombination rates for electron–hole pairs, enhancing

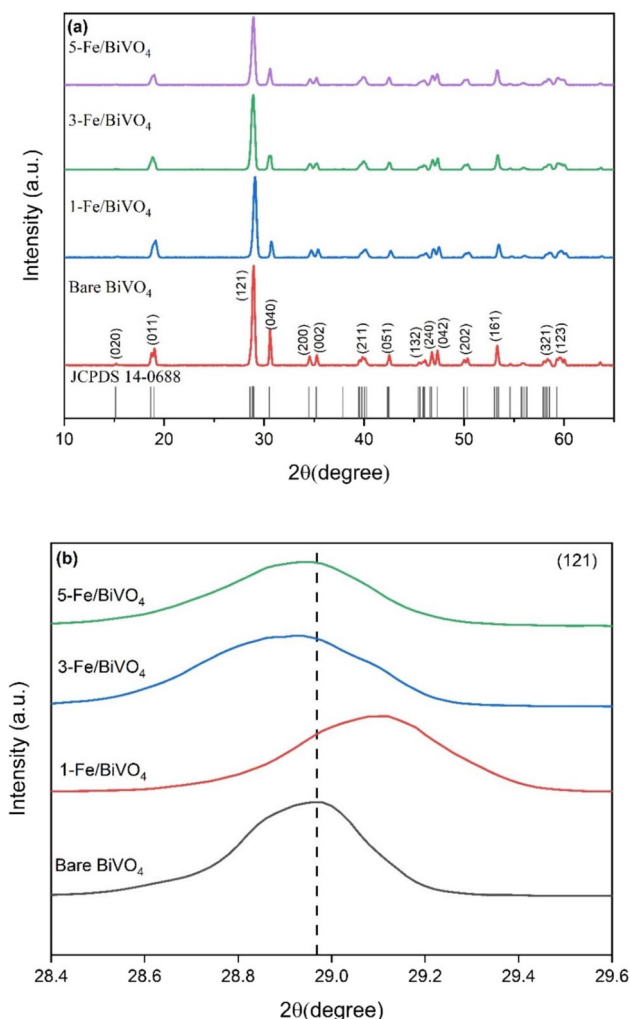


Fig. 3 a XRD patterns of BiVO₄ with various wt% of Fe dopant, b enlarged view of (121) peak at 2θ = 28.8°

Table 1 Calculation of crystallite size, lattice strain and dislocation density for bare and Fe-doped BiVO₄

Photocatalyst	D (nm)	ε	δ = 1/D ²
BiVO ₄	28.8	0.0048	0.0022
1% Fe-doped BiVO ₄	23.6	0.0053	0.0023
3% Fe-doped BiVO ₄	22.3	0.0056	0.0027
5% Fe-doped BiVO ₄	22.4	0.0062	0.0049

photocatalytic efficiency [48]. Lattice strain (ε) and dislocation density (δ) were also calculated to assess structural distortions and defect densities, both of which can impact photocatalytic performance. The lattice strain (ε) was calculated using the following equation (Eq. 3):

$$\epsilon = \beta / 4 \tan \theta \tag{3}$$

and dislocation density (δ) calculated using the following equation (Eq. 4):

$$\delta = 1 / D^2 \tag{4}$$

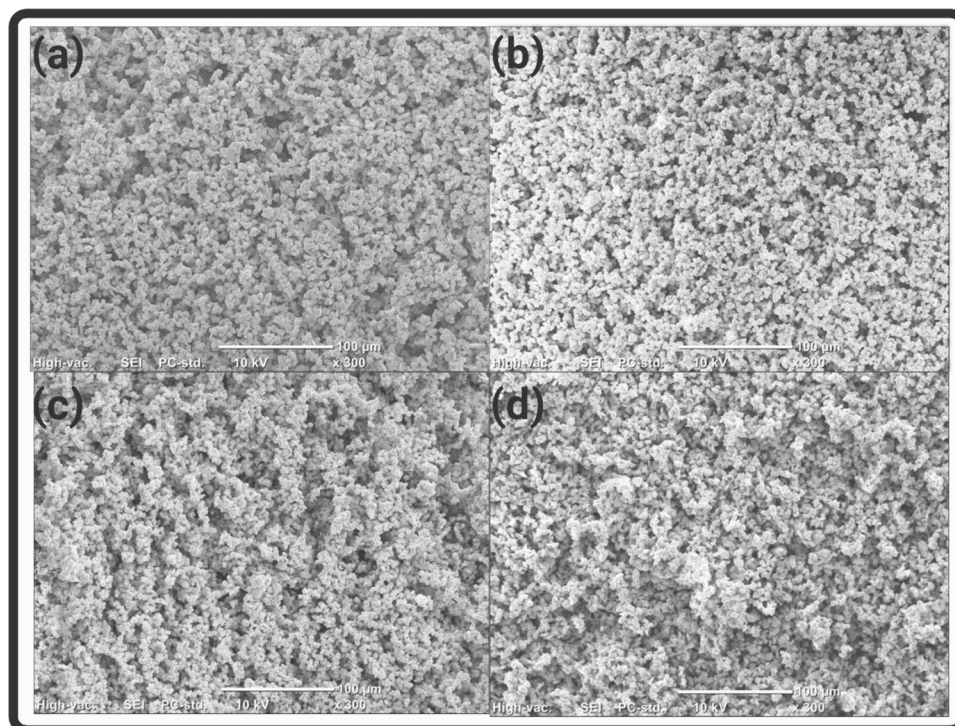
where β is the full width at half maximum (FWHM) value.

Peak broadening is observed with Fe doping, particularly in samples with higher Fe concentrations. This broadening correlates with the reduced crystallite size and increased defect density, consistent with increased lattice strain. Peak broadening further supports the presence of smaller crystallites and strain within the lattice, both of which are favorable for photocatalytic applications by enhancing surface reactivity and light absorption efficiency. It can be seen that lattice strain increases with Fe doping, from 0.0048 in bare BiVO₄ to 0.0062 in 5% Fe-doped BiVO₄. This increase in strain is likely due to the incorporation of Fe ions, which slightly distort the BiVO₄ lattice, enhancing the internal electric field and facilitating charge carrier separation. Increased dislocation density with higher Fe doping concentrations also suggests a rise in defect sites. Defects within the lattice can act as charge traps, extending the lifetime of photogenerated carriers and thus improving photocatalytic performance [49, 50]. The observed structural modifications due to Fe doping specifically reduced crystallite size, increased lattice strain, and higher defect density are advantageous for photocatalytic applications. Smaller crystallites increase the surface area available for photocatalysis, while lattice strain and defect density contribute to improved electron–hole separation, reducing recombination rates and enhancing photocatalytic efficiency.

Scanning electron microscopy (SEM) was used to examine the morphological characteristics of bare and Fe-doped BiVO₄. SEM images presented reveal distinct morphological differences between the bare and Fe-doped BiVO₄. The SEM images of bare BiVO₄ shown in Fig. 4a showed an aggregated, faceted structure with an irregular, worm-like appearance, consistent with previously reported morphologies for BiVO₄ [51].

Upon Fe doping (Fig. 4b–d), noticeable changes in particle morphology are observed. The Fe-doped BiVO₄ samples displayed flakier edges and a more heterogeneous particle distribution, especially in the 1% Fe-doped BiVO₄. These morphological variations indicate that Fe doping may influence particle growth, resulting in more irregular, flake-like structures. The flakier morphology in the Fe-doped samples suggests an increase in surface roughness, which is advantageous for photocatalytic applications, as it potentially increases the availability of reactive sites [52]. Although specific surface area measurements are not available in this study, the observed morphology implies that Fe doping may enhance surface properties, facilitating better pollutant adsorption and light absorption. Additionally, the SEM

Fig. 4 SEM images of BiVO₄ with different wt% of Fe, **a** bare, **b** 1 wt%, **c** 3 wt%, and **d** 5 wt%



images indicate minimal particle aggregation, suggesting that Fe doping does not induce detrimental aggregation that might reduce effective surface area. These structural changes are expected to enhance light absorption and provide more active sites for pollutant interactions, promoting the generation of reactive species, such as $\bullet\text{OH}$. Previous studies have indicated that the presence of Fe in BiVO₄ can alter the crystal structure and morphology, potentially resulting in a flaky morphology that increases the specific surface area. This is essential for improving the photocatalytic performance of the material.

The optical absorption spectra and Tauc plots for Bare BiVO₄ and Fe-doped BiVO₄ samples (1-Fe-BiVO₄, 3-Fe-BiVO₄, and 5-Fe-BiVO₄) are presented in Fig. 5, respectively. The absorbance spectra in Fig. 5a demonstrate a significant improvement in the visible light absorption for Fe-doped BiVO₄ samples compared to bare BiVO₄, indicating enhanced light-harvesting capability as a result of doping. Among the doped BiVO₄ samples, 5-Fe-BiVO₄ exhibited the highest absorbance intensity, suggesting that increasing the Fe content improves the absorption properties of BiVO₄. The redshift observed in the absorption edge of the Fe-doped BiVO₄ samples relative to bare BiVO₄ can be attributed to the introduction of Fe ions into the BiVO₄ lattice [53]. The incorporation of Fe likely creates intermediate energy states within the bandgap, facilitating visible light absorption. This modification aligns with the aim of optimizing BiVO₄'s photoresponse for photocatalytic applications. To further quantify the optical properties, the Tauc plots shown

in Fig. 5b were used to estimate the bandgap energies (E_g) of the materials. The extrapolation of the linear regions of the $(\alpha h\nu)^{0.5}$ vs. $h\nu$ plots yielded bandgap values of 2.78 eV, 2.76 eV, 2.74 eV, and 2.73 eV for bare BiVO₄, 1-Fe-BiVO₄, 3-Fe-BiVO₄, and 5-Fe-BiVO₄, respectively. The reduction in bandgap energy is primarily due to the interaction between Fe 3d orbitals and BiVO₄'s CB and VB. This interaction introduces impurity levels that reduce the energy difference between the conduction band minimum (CBM) and valence band maximum (VBM). Consequently, the optical transition from the VB to the CB occurs at lower photon energies in Fe-doped BiVO₄.

3.1.1 Photodegradation Test

The photocatalytic degradation of TC under low-power UV irradiation was investigated using bare and Fe-doped BiVO₄ photocatalysts, as shown in Fig. 6. The degradation performance was monitored by the concentration ratio (C/C_0), where C_0 represents the initial concentration of TC, and C is the concentration at different time intervals. Figure 6a demonstrates the variation of TC concentration over time under both dark and light conditions. In the dark phase (0–30 min), no significant reduction in TC concentration was observed for any of the photocatalysts, indicating minimal adsorption of TC onto the photocatalyst surfaces. This behavior confirms that the degradation mechanism is predominantly photocatalytic and not due to adsorption. Upon exposure to light, the degradation of TC is significantly

Fig. 5 **a** UV–vis absorption spectra of bare and various wt% of Fe-doped BiVO₄, **b** Tauc plot with the corresponding band gap energies

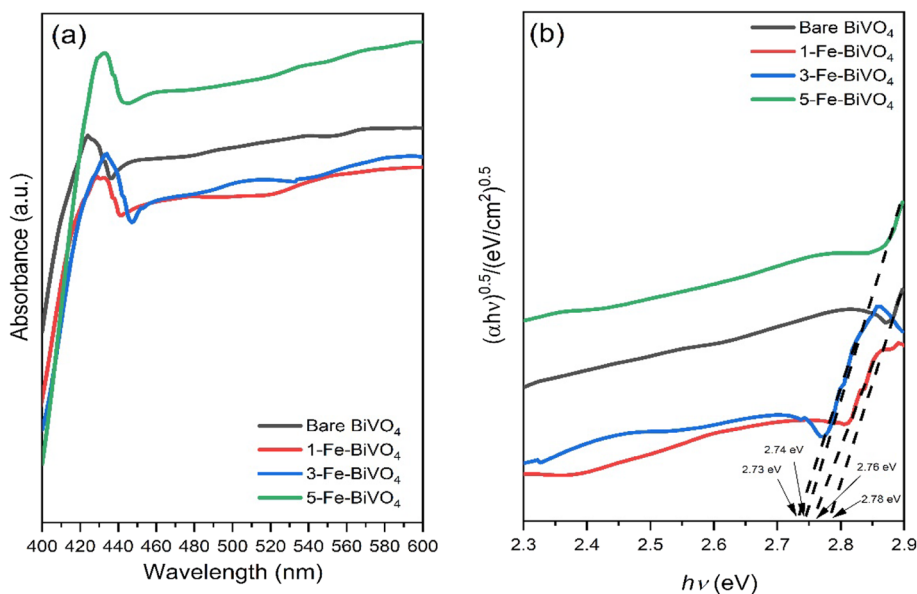
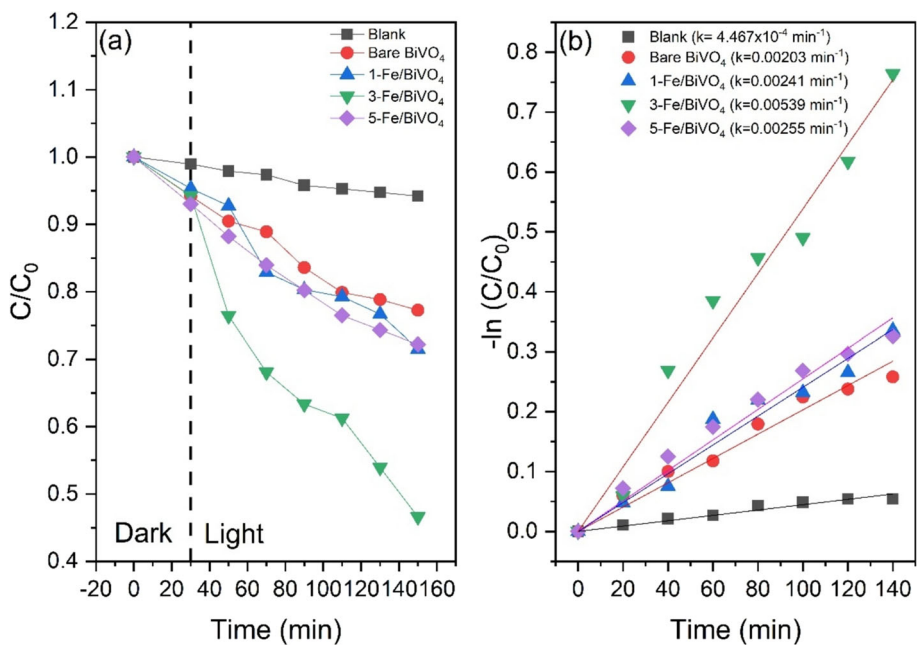


Fig. 6 Photocatalytic degradation of TC under low-power UV light using bare and Fe-doped BiVO₄. **a** Degradation profiles showing TC concentration (C/C_0) vs. time for different photocatalysts under dark and UV irradiation. **b** Kinetic plots based on PFO model fitting with corresponding rate constants ($-\ln(C/C_0)$ vs. time)

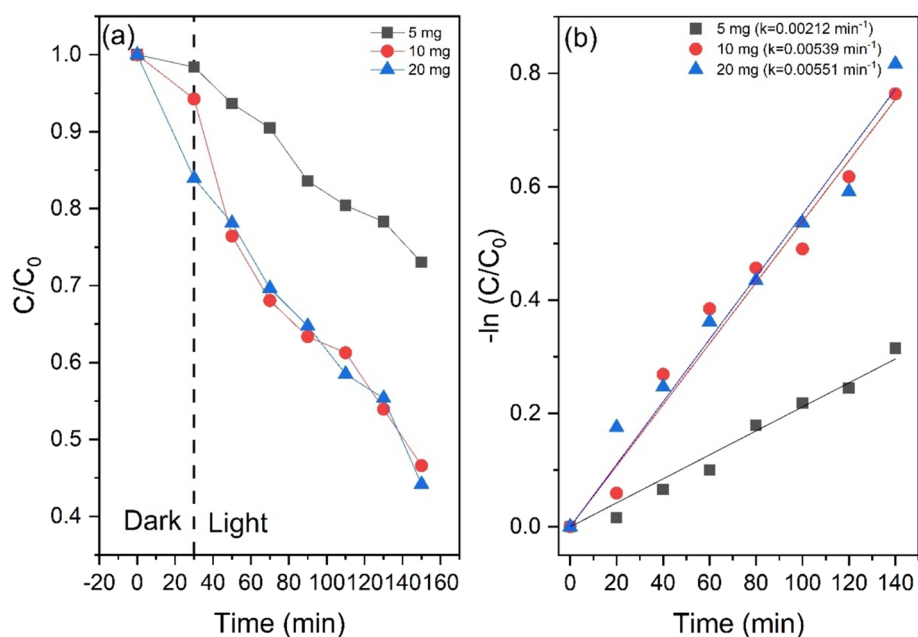


enhanced, particularly for Fe-doped BiVO₄ samples. Among the tested photocatalysts, 3 wt% Fe-doped BiVO₄ exhibited the highest TC degradation efficiency, achieving 73.37% within 120 min. In contrast, bare BiVO₄ and other Fe-doped samples (1 wt% and 5 wt%) showed relatively moderate photocatalytic activities. The blank experiment (without a photocatalyst) resulted in negligible degradation, confirming the necessity of a photocatalyst for TC degradation under low-power UV irradiation. Additionally, photolysis experiments, where TC was exposed without the addition of photocatalysts, showed very minimal degradation, emphasizing that direct photolysis is insufficient for effective TC removal under these conditions. Figure 6b presents the

kinetic plots of $\ln(C/C_0)$ versus time for TC degradation. The data was fitted to a PFO kinetic model, and the apparent rate constants (k) for each photocatalyst were determined. The highest rate constant was observed for 3 wt% Fe-doped BiVO₄, which was approximately 2.65 times higher than that of bare BiVO₄, demonstrating enhanced photocatalytic efficiency due to improved charge separation and surface reactivity. This enhancement highlights the critical role of Fe doping in accelerating photocatalytic reactions. Bare BiVO₄, while moderately active, exhibited a much lower rate constant, indicating its limited capability in harnessing low-power UV light for photocatalysis. The blank experiment showed a negligible rate constant, further emphasizing

Fig. 7 Effect of catalyst loading on the photocatalytic degradation of TC using 3% Fe-doped BiVO₄ under 13 W UV light.

a Degradation efficiency at different catalyst dosages (5 mg, 10 mg, and 20 mg). **b** PFO kinetic plots for each loading condition with calculated rate constants



the photocatalytic nature of the degradation process. The 3 wt% Fe doping optimally enhances the photocatalytic reaction rate, likely due to improved charge carrier dynamics and increased ROS generation. The trend observed here is consistent with similar studies on metal-doped BiVO₄ systems, where intermediate dopant levels provide an optimal balance of enhanced light absorption and minimized recombination. Previous studies on transition metal doping in BiVO₄ confirm that moderate doping concentrations, such as the 3% Fe level used here, effectively introduce beneficial electronic states without overwhelming the material with recombination centers [54, 55]. However, as Fe doping increases beyond 3%, excess Fe ions can act as recombination centers, reducing photocatalytic efficiency by increasing electron–hole recombination rates. This explains why the 5 wt% Fe-doped BiVO₄, with a rate constant of only 0.0072 min^{-1} , underperforms compared to the 3% Fe-doped BiVO₄. The improved photocatalytic activity at 3% Fe doping is also supported by SEM analysis, which shows that Fe doping at this concentration enhanced surface morphology, resulting in a flakier structure with increased surface roughness. These morphological changes increase the specific surface area, facilitating pollutant adsorption and providing more active sites for photocatalytic reactions. While the photocatalytic degradation data were fitted using a PFO kinetic model, it is important to acknowledge certain limitations of this approach. The model assumes a constant number of active sites and homogeneous reaction conditions, which may not fully reflect the dynamic surface interactions and intermediate species formation in heterogeneous photocatalysis [56, 57]. Additionally, deviations from linearity at later stages of degradation may occur

due to the accumulation of intermediates or catalyst deactivation.

The effect of different catalyst loadings of 3% Fe-doped BiVO₄ on the photocatalytic degradation of TC was examined, as shown in Fig. 7. Catalyst loadings of 5 mg, 10 mg, and 20 mg were used to assess their impact on degradation efficiency and reaction kinetics. Figure 7a illustrates the degradation profiles of TC under various catalyst loadings. Upon exposure to low-power UV light, the degradation rate improved markedly with increasing catalyst loading, reaching an optimal performance at 10 mg. Higher photocatalyst amount enhanced surface area and active sites, allowing more pollutant molecules and light photons to interact with the photocatalyst, which boosts electron excitation and increases the production of ROS [58]. Conversely, at a lower loading of 5 mg, the degradation efficiency was significantly reduced due to insufficient active sites for photocatalysis. Interestingly, increasing the catalyst loading to 20 mg did not result in further improvement; instead, a slight reduction in efficiency was observed, likely due to light scattering and shielding effects that hinder photon penetration. The highest rate constant was observed for the 20 mg catalyst (0.00551 min^{-1}) loading as shown Fig. 7b, highlighting its superior performance in facilitating the photocatalytic degradation of TC.

The influence of initial solution pH on the photodegradation of TC was studied using 3% Fe-doped BiVO₄, as shown in Fig. 8. Three pH levels (4, 7, and 9) were selected to evaluate the effect of acidic, neutral, and alkaline conditions. Figure 8a indicates that the optimal pH for TC photocatalytic degradation using 3% Fe-doped BiVO₄ occurs in acidic conditions (pH 4). This pH level significantly enhances photocatalytic activity compared to neutral (pH 7) and basic

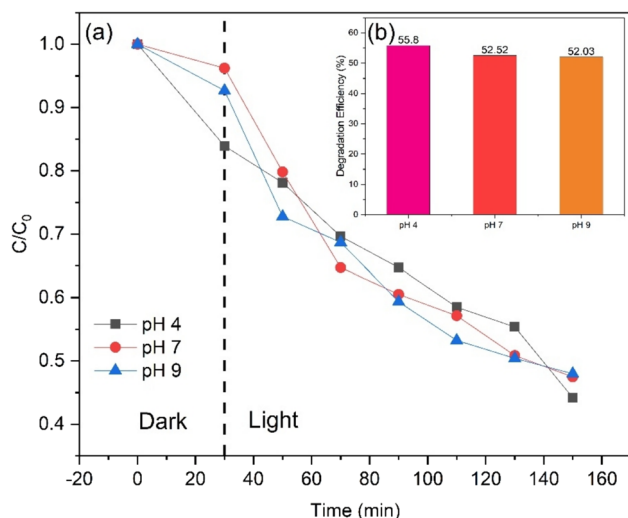


Fig. 8 a Effect of initial solution pH on TC photodegradation. b degradation efficiency at different pH

(pH 9) conditions. In acidic environments, the increased concentration of protons enhances electrostatic interactions between the positively charged surface of the photocatalyst and negatively charged TC molecules [59–61]. This attraction improved the adsorption of TC onto the photocatalyst, which is crucial for effective degradation. At pH 9, both the photocatalyst and TC carry negative charges, leading to repulsion that reduces interaction and thus diminishes photocatalytic performance. The electrostatic repulsion between the negatively charged photocatalyst surface and TC molecules may reduce the adsorption efficiency, leading to slightly lower degradation rates. Lower pH levels facilitate the generation of ROS, such as $\bullet\text{OH}$, which are pivotal in the degradation process as shown in Fig. 8b (inset). Studies have shown that these radicals are produced more effectively in acidic conditions, enhancing the oxidative capacity of the photocatalytic system [62].

Figure 9a depicts the degradation profiles of TC at different initial concentrations. At lower concentrations (5 mg L^{-1}), the photocatalyst demonstrated the highest degradation efficiency. As the initial concentration increased to 10 mg L^{-1} and 20 mg L^{-1} , the degradation rate decreased, indicating an inverse relationship between TC concentration and photocatalytic efficiency. This trend is attributed to the reduced availability of active sites on the photocatalyst surface at higher pollutant concentrations, leading to competition among TC molecules for adsorption and subsequent degradation. Another explanation is that as the photocatalytic reaction develops, various degradation intermediates formed in high-concentration TC solution would compete with TC molecules for active photocatalytic sites on the catalyst surface, inhibiting the generation of reactive species [54, 63]. The kinetic plots shown in Fig. 9b confirm a PFO reaction,

with the apparent rate constants (k) determined as follows: 5 mg L^{-1} : 0.00852 min^{-1} ; 10 mg L^{-1} : 0.00551 min^{-1} and 20 mg L^{-1} : 0.00239 min^{-1} . The highest rate constant was observed at the lowest concentration (5 mg L^{-1}), consistent with the greater efficiency of the photocatalytic process under dilute conditions. As the concentration increased, the rate constant decreased, likely due to limited light penetration and overshadowing effects caused by higher TC concentrations.

The role of ROS in the photodegradation of TC was investigated by employing different scavengers, as shown in Fig. 10a. Scavengers such as EDTA, ascorbic acid, methanol, and tert-butanol were used to selectively quench holes (h^+), superoxide radicals ($\bullet\text{O}_2^-$), and hydroxyl radicals ($\bullet\text{OH}$), respectively. Without any scavenger, the degradation efficiency reached 73.38%, highlighting the effectiveness of the photocatalyst in the absence of ROS quenching. Upon the addition of EDTA, which selectively scavenges h^+ , the degradation efficiency dropped to 46.09%, indicating the significant role of h^+ in the degradation process. Similarly, ascorbic acid, a scavenger for $\bullet\text{O}_2^-$, reduced the efficiency to 39.17%, suggesting that O_2^- also contributes substantially to the degradation mechanism. Methanol and tert-butanol, which scavenge $\bullet\text{OH}$, resulted in degradation efficiencies of 22.03% and 43.1%, respectively. The pronounced reduction in degradation efficiency upon methanol addition indicated the predominant role of $\bullet\text{OH}$ as the major ROS responsible for TC photodegradation.

The reusability of 3% Fe-doped BiVO_4 for TC degradation was evaluated over three consecutive cycles under as shown in Fig. 10b. The degradation performance and efficiency were monitored to assess the stability and durability of the photocatalyst. In the first cycle, the photocatalyst exhibited a degradation efficiency of 73.39%, which slightly decreased to 72.19% in the second cycle and 63.51% in the third cycle. The reduction in efficiency after multiple cycles can be attributed to photocatalyst deactivation, possibly caused by surface fouling, active site blocking, or partial structural degradation [64]. The observed decline in degradation efficiency suggests that the 3% Fe-doped BiVO_4 undergoes minor deactivation during reuse. Factors contributing to this deactivation may include the accumulation of by-products or residual TC molecules on the catalyst surface, which inhibits active site accessibility. Additionally, prolonged exposure to light and reaction intermediates could lead to partial degradation of the photocatalyst's structure or active sites. Despite this decline, the photocatalyst retains a relatively high efficiency, demonstrating its potential for multiple reuse cycles with minimal performance loss. Future works could assess the stability of this catalyst in continuous flow systems, which would further support its application in real-world conditions. Some photocatalysts, especially metal oxides, can undergo photocorrosion, where the material is

Fig. 9 Effect of initial TC concentration on photocatalytic degradation using 3% Fe-doped BiVO₄. **a** TC degradation profiles at concentrations of 5 mg/L, 10 mg/L, and 20 mg/L. **b** PFO kinetic plots for each loading condition with calculated rate constants

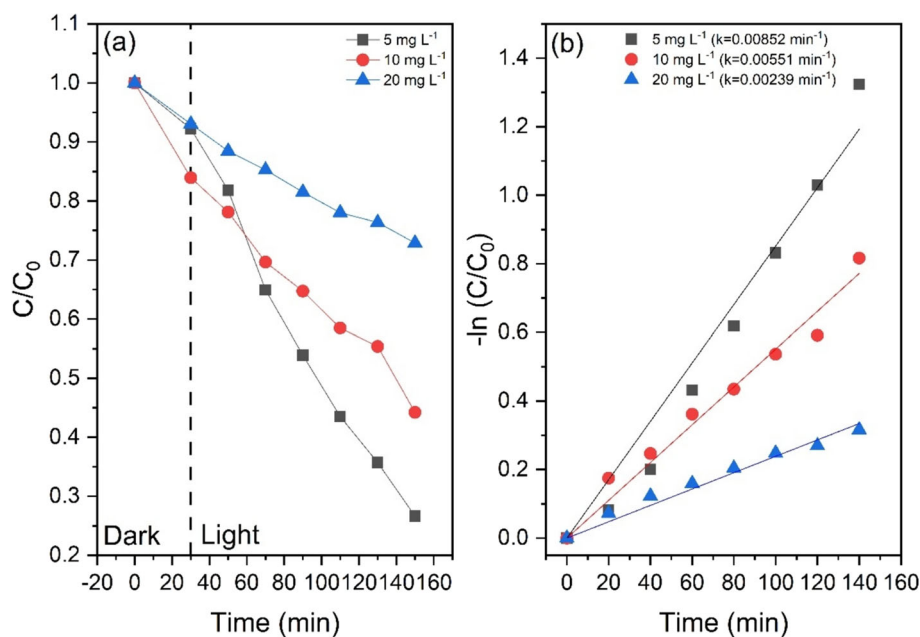
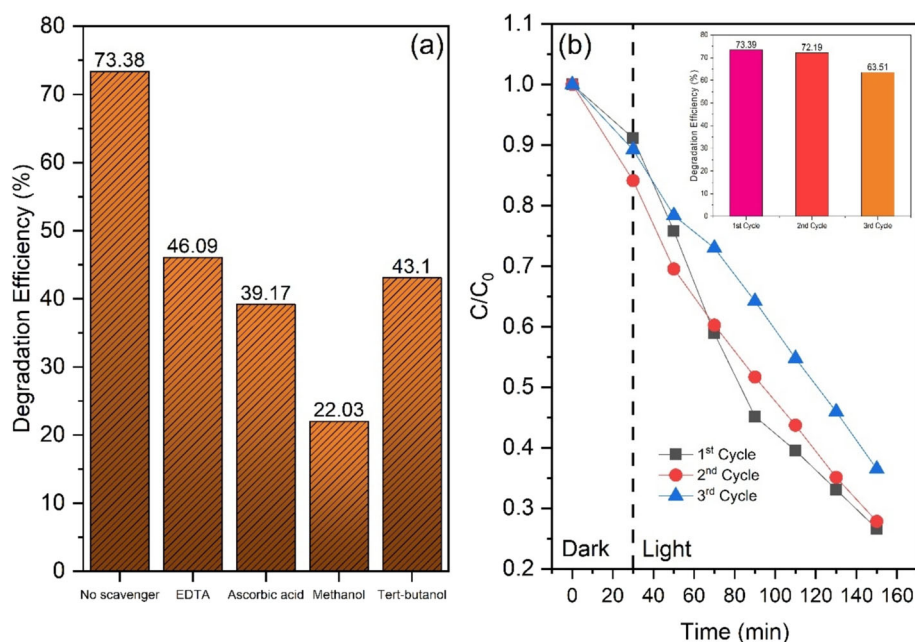


Fig. 10 a Photodegradation efficiency after the addition of various scavengers. **b** Reusability of the 3% Fe-doped BiVO₄ for TC photodegradation. *Inset:* Degradation efficiency of 3% Fe-doped BiVO₄ after 3 cycles



chemically degraded under light irradiation. This can result in the loss of active sites and reduced catalytic activity [65].

A comparative analysis of the FTIR spectra of 3% Fe-doped BiVO₄ before and after TC degradation shown in Fig. S2 further proved that no TC was adsorbed on the surface of the photocatalyst. Comparing the FTIR spectra of fresh and post-degradation Fe-doped BiVO₄ highlights the structural stability of the catalyst's functional groups, with minimal chemical changes observed. The main functional groups, especially the O–H and V–O–V bands critical for photocatalysis, are preserved, demonstrating the catalyst's stability. The peak around 1600 cm⁻¹ can be attributed to the

bending vibration of water molecules. No significant shifting of the peak ascribed to the V–O–V bonds, indicating the stability of the photocatalyst even after 3 cycles of photodegradation. These findings suggest that the photocatalytic process involves the activation of the hydroxyl groups on the surface of the BiVO₄ catalyst. The hydroxyl groups may react with the TC molecules, leading to their degradation.

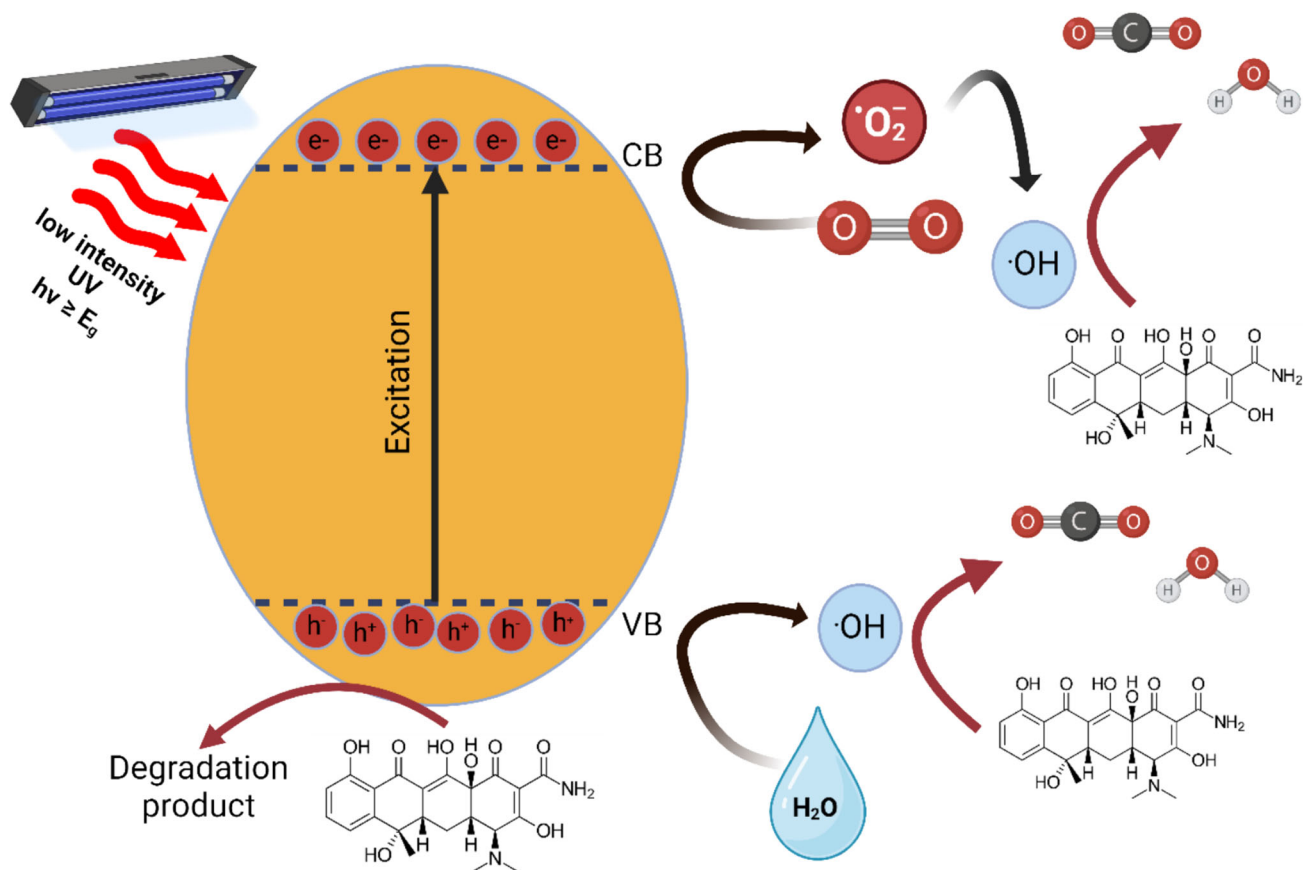
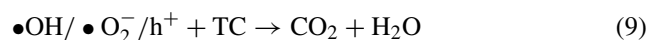


Fig. 11 Proposed TC degradation mechanism

3.1.2 Proposed Mechanism Degradation of TC

A possible photocatalytic degradation mechanism for 3% Fe-doped $BiVO_4$ under low-power intensity UV light irradiation can be proposed as shown in Fig. 11. When UV light irradiates the $BiVO_4$, it provides energy to excite electrons from the VB to the CB, creating electron-hole pairs (e^-/h^+). The presence of 3% Fe doping likely enhances this process by improving charge separation, which prevents the rapid recombination of the electron-hole pairs. Fe^{3+} ions (with partially filled 3d orbitals) are known to introduce shallow trap states within the bandgap of $BiVO_4$. These trap states act as intermediate energy levels between the VB and CB, capturing photogenerated electrons and thereby reducing the rate of electron-hole recombination. This mechanism effectively prolongs carrier lifetimes, enhances ROS formation, and improves overall photocatalytic performance [66, 67]. Furthermore, the Fe doping lowered the bandgap energy to approximately 2.69 eV, facilitating the formation of ROS. The h^+ generated in the VB can interact with water molecules (H_2O) or hydroxide ions (OH^-) to produce highly reactive $\cdot OH$. These radicals are key to the degradation process as they are potent oxidizing agents. Based on radical trapping

experiments, the primary ROS involved in this mechanism are $\cdot OH$ and h^+ , which play significant roles in breaking down the pollutant molecules. In addition to $\cdot OH$, $\cdot O_2^-$ may also be generated and contribute to the oxidative degradation. Both of these ROS can attack and oxidize the TC, leading to its breakdown into less harmful compounds or complete mineralization. Therefore, the combined effect of charge separation and the generation of ROS makes the 3% Fe-doped $BiVO_4$ an effective photocatalyst under UV light for pollutant degradation. The mechanism regarding the degradation of TC can be expressed as:



The degradation pathway of TC can be tentatively proposed based on prior research [68]. ROS particularly $\bullet\text{OH}$ radicals play a critical role in attacking the aromatic rings of TC. One study proposed that the degradation starts with the demethylation, followed by deamination and dihydroxylation reactions [69]. The cleavage of carbon–carbon bonds and ring-opening reactions is also expected from the radicals involved. The likely degradation pathway begins with the fragmentation of the aromatic structure to produce intermediates such as 1-ethyl-6-methylidencyclohexa-1,4-diene, followed by further oxidation to generate compounds like 5,6-dimethylidencyclohexa-1,3-diene. Subsequent $\bullet\text{OH}$ radical attacks lead to the formation of dienal and dienol intermediates, which eventually break down into smaller organic molecules such as propanol. The complete mineralization of TC to CO_2 and H_2O is suggested as the final step in the degradation pathway. While no total organic carbon (TOC) measurements were conducted in this study, prior work indicates that photocatalytic systems with effective ROS generation achieve high levels of mineralization.

3.1.3 Degradation Performance of TC Using Various Bi Based Photocatalysts

The performance of 3% Fe-doped BiVO_4 in degrading TC was assessed alongside various Bi-based photocatalysts from previous studies, as summarized in Table 2. This comparison highlights the relative efficiency of Fe-doped BiVO_4 under low-intensity UV light and identifies the factors contributing to its competitive photocatalytic activity. The 3% Fe-doped BiVO_4 achieved a degradation efficiency of 73.37% under low-power (13 W) UV irradiation over 120 min. When compared to other Bi-based photocatalysts, Fe-doped BiVO_4 demonstrates a comparable or superior degradation performance, particularly under modest light conditions. For instance, BiVO_4/Z -type $\text{BiOI}/\text{g-C}_3\text{N}_4$ composites exhibit higher degradation efficiencies (e.g., 95.63%) under sunlight, and $\text{Bi}_2\text{O}_3/\text{Sb}_2\text{S}_3$ achieves 91.5% under solar light. However, these systems often rely on more intense light sources or additional components, whereas Fe-doped BiVO_4 performs effectively with a simpler, low-power UV setup, making it more practical for cost-effective applications. Different strategies, including metal doping and heterojunction formation, enhance photocatalytic efficiency by increasing light absorption, improving electron–hole separation, and facilitating ROS generation. In the case of 3% Fe-doped BiVO_4 , Fe doping introduces intermediate energy levels within the band gap. This not only shifts the absorption edge into the visible range, but also enhances charge carrier dynamics, allowing for efficient electron–hole separation and reduced recombination. Compared to more complex composite systems, Fe doping alone provides a straightforward yet effective means to improve BiVO_4 's photocatalytic activity without

requiring intricate synthesis steps. The degradation of TC using Fe-doped BiVO_4 is primarily driven by the generation of ROS, such as $\bullet\text{OH}$ and $\bullet\text{O}_2^-$. The presence of Fe ions facilitates the formation of these ROS by enhancing electron transfer processes and stabilizing charge carriers. In contrast, some Bi-based composites such as CdS-doped SiO_2/BiOX generate ROS through the combined effect of multiple semiconductors, which often requires precise synthesis control to maintain stability. Fe-doped BiVO_4 , however, achieves effective ROS generation with a single doping element, offering a simpler and more stable alternative. One of the most notable advantages of 3% Fe-doped BiVO_4 is its high degradation efficiency under low-intensity UV light, which reduces operational costs and energy requirements. Additionally, Fe-doped BiVO_4 demonstrates strong stability and reusability over multiple cycles, with minimal degradation in performance, making it suitable for long-term applications.

In contrast to many Bi-based photocatalytic systems that rely on complex heterojunction architectures or incorporate rare and expensive metals such as Ag, Au, or Cd, the Fe-doped BiVO_4 developed in this study offers a simpler, more economical alternative with competitive photocatalytic efficiency. Notably, while BiVO_4/Z -type $\text{BiOI}/\text{g-C}_3\text{N}_4$ composites have been reported to achieve up to 95.63% TC degradation under natural sunlight, they require multistep synthesis and structural tuning. By comparison, the 3 wt% Fe-doped BiVO_4 achieves 73.37% degradation under a low-power 13 W UV lamp, representing a significant reduction in energy input while maintaining effective pollutant removal. This improvement reflects the enhanced charge separation and light harvesting conferred by Fe incorporation.

The catalyst's single-phase structure and hydrothermal synthesis route simplify scale-up and reduce production costs, making it particularly suitable for decentralized or off-grid wastewater treatment systems especially in resource-limited or rural settings. Furthermore, the hydrothermal method employed is readily adaptable for industrial-scale fabrication and can be integrated into existing water treatment infrastructure without requiring advanced instrumentation or post-synthesis modification [76, 77].

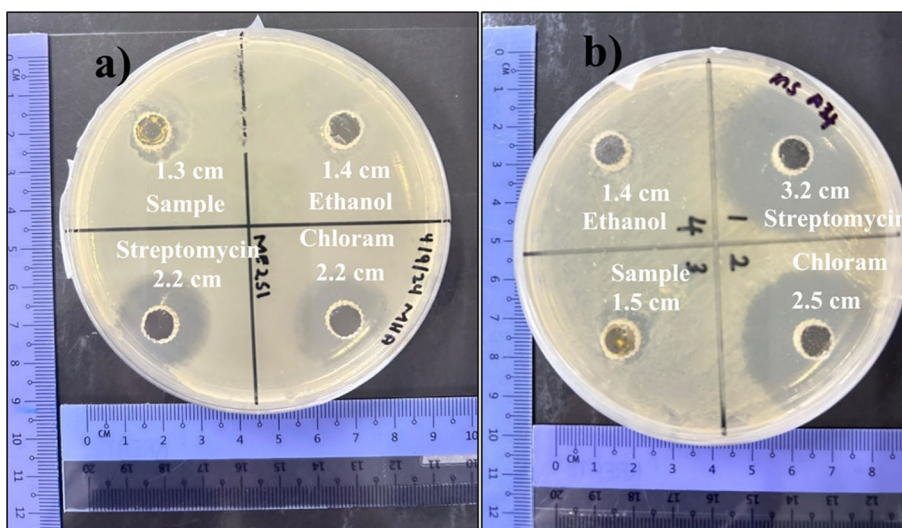
Although this study was designed to evaluate performance under low-intensity UV irradiation, simulating low-energy operational environments, it is recognized that Fe doping also enhances visible light absorption, as indicated by the red-shift in the UV–vis absorption spectra (Fig. 5a). Thus, future investigations should assess photocatalytic activity under visible light illumination using white LED arrays or solar simulators. This would validate the material's functionality under broader environmental conditions and allow direct performance comparisons with other visible-light-responsive catalysts. Expanding the light-source scope will be essential to fully establish the material's versatility and practical relevance for real-world applications.

Table 2 Reported performance of Bi-based photocatalysts toward degradation of TC pollutants

Pollutants	Concentration	Photocatalyst	Light source/time	Degradation efficiency (%)	References
OTC	10 mg/L	BiVO ₄	Sunlight / 240 min	83	[70]
TC and OTC	10 ppm	BiVO ₄	Sunlight / 240 min	72 and 83	[29]
TC	10.94 mg/L	Z-type BiOI/g-C ₃ N ₄	Sunlight / 150 min	95.63	[71]
OF and TC	10 mg/L	CdS-doped SiO ₂ @BiOX (X = Br, Cl)	Simulated sunlight / 60 min	100 and 86.8	[72]
TC	0.3 g/L	Bi ₂ O ₃ /Sb ₂ S ₃	Solar light illumination / 120 min	91.5	[73]
TC and CIP	20 mg/L and 10 mg/L	SnS ₂ /Bi ₂ WO ₆	Natural sunlight / 90 min	97 and 93	[74]
TC	40 mg/L	BiVO ₄ /CuBi ₂ O ₄	Simulated sunlight / 180 min	85	[75]

TC, tetracycline; OTC, oxytetracycline; CIP, ciprofloxacin; OF, ofloxacin

Fig. 12 Zone of inhibition (ZOI) formed by 3% Fe-doped BiVO₄ against **a** *E. coli* and **b** *S. aureus*



3.1.4 Antimicrobial Activity

Photocatalysts that demonstrate the ability to inactivate bacteria can play a significant role in preventing the proliferation of pathogenic microorganisms, thereby enhancing the safety of treated water. In this study, the antibacterial efficacy of 3% Fe-doped BiVO₄ was evaluated by testing its ability to inactivate *E. coli* and *S. aureus*, as illustrated in Fig. 12 and summarized in Table 3. To compare the antibacterial efficacy of the 3% Fe-doped BiVO₄ photocatalyst, chloramphenicol and streptomycin were employed as positive controls. Chloramphenicol exhibited notable ZOI, with measurements of

Table 3 ZOI for the 3% Fe-doped BiVO₄

Sample	<i>E. coli</i>	<i>S. aureus</i>
3% Fe-doped BiVO ₄	0.45 ± 0.697	1.33 ± 0.216
Positive control Streptomycin	2.24 ± 0.291	3.35 ± 0.193
Positive control Chloramphenicol	2.14 ± 0.151	2.90 ± 0.298
Negative control Ethanol	0.00 ± 0.00	1.19 ± 0.196

2.14 ± 0.151 cm and 2.90 ± 0.298 cm, respectively. Streptomycin demonstrated similar antibacterial activity, with ZOI values of 2.24 ± 0.291 cm for *E. coli* and 3.35 ± 0.193 cm for *S. aureus*. In contrast, no ZOI was observed in the negative control (95% ethanol) on the *E. coli* plate, indicating no antibacterial activity. For *S. aureus*, the ZOI for ethanol was measured at 1.19 ± 0.196 cm. The observed disparity between the effects of ethanol on *E. coli* and *S. aureus* can likely be attributed to structural differences between the two bacteria [78]. The outer membrane of Gram-negative bacteria is composed of lipopolysaccharides in the outer leaflet and glycerophospholipids in the inner leaflet, creating a highly ordered structure that effectively limits the permeability of hydrophobic compounds, such as ethanol [79]. The ZOI values for *E. coli* and *S. aureus* were found to be 0.45 ± 0.697 cm and 1.33 ± 0.216 cm for 3% Fe-doped BiVO₄, respectively. These results suggest that the photocatalyst exhibits a moderate antibacterial effect, with greater efficacy against *S. aureus* compared to *E. coli*. The antibacterial activity of 3% Fe-doped BiVO₄ can be explained via two distinct physical and chemical processes, both of which are linked to its surface oxygen groups [78]. Physical force is exerted by oxygen groups directly attaching to bacterial cell walls.

As shown in Table 3, the 3% Fe-doped BiVO₄ showed greater inhibitory activity against *S. aureus* (1.33 ± 0.216 cm) than *E. coli* (0.45 ± 0.697 cm), suggesting differential interaction with Gram-positive vs. Gram-negative bacteria. While the differences are apparent, formal hypothesis testing (e.g., t test or ANOVA) was not conducted in this study due to small sample size and the preliminary scope of the antibacterial assessment. Future work will incorporate expanded replicates and detailed statistical testing to confirm these observations. In addition, future investigations will be expanded to include a broader spectrum of waterborne pathogens. Comparative antibacterial assessments under visible light or solar-simulated irradiation should be conducted to fully explore the material's dual-function capability for pollutant degradation and microbial disinfection under real-world operational conditions.

3.1.5 Cost Analysis and Practical Feasibility

For a photocatalyst to be viable in real-world applications, cost-efficiency is a critical factor alongside photocatalytic performance and stability. Table 4 provides an estimate of the costs associated with synthesizing 3% Fe-doped BiVO₄, taking into account the primary raw materials, and the required synthesis steps. The total synthesis cost per batch for 3% Fe-doped BiVO₄ is estimated at approximately RM 8.17/g. The key raw materials include bismuth nitrate pentahydrate, ammonium metavanadate, and iron (II) sulfate as the Fe source. These materials are relatively inexpensive, especially when compared to more complex or precious

metals commonly used in photocatalysis. The low cost of Fe as a dopant further supports the economic feasibility of this photocatalyst. The synthesis of 3% Fe-doped BiVO₄ involves a straightforward hydrothermal method, which can be implemented with standard laboratory equipment, including a Teflon-lined autoclave. The process involves moderate heating (180 °C for 15 h) and does not require specialized reagents, making it accessible and scalable. When calculating energy consumption for heating and autoclave operation, the synthesis cost per gram of Fe-doped BiVO₄ remains low, which is beneficial for scaling the process to industrial levels.

Additionally, the straightforward recovery process for the catalyst (using centrifugation or filtration, followed by simple washing) adds to its economic appeal, as it does not require costly or complex regeneration steps. The high repeatability and stability of 3% Fe-doped BiVO₄, as demonstrated in multiple photocatalytic cycles, minimize the need for frequent replacement. This reusability reduces the overall operating cost in wastewater treatment applications, allowing the catalyst to be used repeatedly without significant loss of efficiency. Given its stable performance and minimal deactivation across cycles, the cost per use decreases over time, making it an economically favorable choice for long-term water treatment. Compared to other Bi-based and metal-doped photocatalysts, such as TiO₂, Ag-doped ZnO, and composite materials, Fe-doped BiVO₄ offers a lower-cost alternative with competitive photocatalytic performance.

Although the estimated synthesis cost of 3% Fe-doped BiVO₄ was RM 8.17/g at laboratory scale, this figure is expected to drop substantially under industrial-scale production. Bulk procurement of raw materials, enhanced thermal management, and increased batch throughput typically reduce per-unit energy consumption and overall process costs. Based on conservative scale-up projections, the production cost could be lowered to approximately RM 3.50–4.00/g, assuming standard economies of scale and continuous hydrothermal operation [80].

When compared to other common photocatalysts, Fe-doped BiVO₄ remains competitively priced. While materials such as TiO₂ and ZnO are lower in raw material cost, they require high-intensity UV sources (≥ 100 W) to achieve substantial degradation efficiencies. This leads to higher operational energy demands. In contrast, 3% Fe-doped BiVO₄ achieves 73.37% TC degradation under a mere 13 W UV lamp, making it highly attractive for low-energy or off-grid applications. More sophisticated photocatalysts like Ag/ZnO or rare-earth doped systems, though effective under visible light, often exceed RM 20–50/g due to the use of noble metals and synthesis complexity.

The practical implications of this are particularly relevant for industrial wastewater treatment systems, especially for the removal of persistent pharmaceutical pollutants such as TC. Its high photocatalytic efficiency under low-intensity UV

Table 4 Estimated costs involved in the synthesis of 3% Fe-doped BiVO₄ photocatalyst

Item	Quantity (per batch)	Unit Cost (RM)	Total Cost (RM)	Notes
<i>Raw materials</i>				
Bi(NO ₃) ₃ ·5H ₂ O	3.3954 g	2.38/ g	8.08	Main Bi source
NH ₄ VO ₃	0.8189 g	1.25/ g	1.02	Main V source
FeSO ₄ ·7H ₂ O	0.101 g	0.098/ g	0.01	Fe dopant source
Total raw material cost			9.11	
<i>Synthesis process</i>				
Hydrothermal heating (180 °C)	1.5 kWh X 15 h = 22.5 kWh	0.24 per kWh*	5.40	Energy cost for autoclave operation
Deionized water	200 mL	0.01/mL	2.00	For dissolving reagents and washing catalyst
Ethanol (for washing)	20 mL	0.11/ mL	2.20	For catalyst washing
Drying	1.5 kWh X 12 h = 18.0 kWh	0.24 per kWh*	4.32	Energy cost for oven operation
Calcination	3.0 kWh X 4 h = 12.0 kWh	RM 0.24 per kWh*	2.88	Energy cost for box furnace operation
Total Synthesis Cost			16.80	
<i>Equipment depreciation</i>				
Teflon-lined autoclave usage	–	–	1.40	Based on estimated equipment depreciation per batch
Centrifuge/filtration setup	–	–	1.30	Equipment for recovery and filtration
Total equipment cost			2.70	
Overall cost			28.61	Per batch (3.5 g photocatalyst yield)

*Refer to Sarawak Energy, Malaysia tariff rate

light supports its integration into decentralized systems such as solar-assisted reactors or mobile water purification units in rural or energy-constrained environments. Furthermore, the intrinsic antibacterial activity of Fe-doped BiVO₄, even under dark conditions, adds value as a dual-function material capable of both pollutant degradation and microbial disinfection.

4 Conclusion

In conclusion, this study successfully demonstrates the potential of Fe-doped BiVO₄ as an effective photocatalyst for the degradation of TC. The synthesis of bare and Fe-doped BiVO₄ using the hydrothermal method resulted in a monoclinic-tetragonal heterostructure with crystallite size of 27.37 – 29.10 nm. The obtained band gap is between the range of 2.69–2.87 nm. This study showed the importance of optimizing both the Fe doping concentration and the catalyst loading to achieve the best photocatalytic activity. Photocatalytic tests showed that the 3% Fe-doped BiVO₄ had the highest degradation efficiency for TC, achieving a removal rate of 73.37% under low-power (13 W) UV lamp in 120 min.

The increased photoactivity was attributed to improved electron–hole separation and an optimized Fe doping concentration, highlighting the catalyst's potential for environmental remediation applications. Stability and reusability studies demonstrated that 3% Fe-doped BiVO₄ maintained high photocatalytic performance over three cycles with minimal loss in activity. This stability under repeated use suggests that Fe-doped BiVO₄ is a viable candidate for long-term application in water treatment. This highlights the Fe-doped BiVO₄ effectiveness in addressing antibiotic-based pollution, even under low light intensity. In addition, the antibacterial activity of 3% Fe-doped BiVO₄ was further evaluated, expanding its potential applications. Antibacterial tests revealed an inhibition zone against *S. aureus*, suggesting that the catalyst not only effectively degrades pollutants under low-intensity UV light, but also exhibits antibacterial properties in the dark. These combined attributes make Fe-doped BiVO₄ a promising material for practical applications in wastewater treatment and environmental remediation. The cost analysis revealed that the synthesized Fe-doped BiVO₄ costs RM 8.17 per gram, further enhancing its appeal for scalable and cost-effective applications.



Supplementary Information The online version contains supplementary material available at <https://doi.org/10.1007/s13369-025-10278-8>.

Acknowledgements This work was supported by Universiti Putra Malaysia Grant GP-IPM/9750400. The authors confirm that there are no additional funders. The funder had no role in study design, data collection and analysis, decision to publish, or preparation of the manuscript. The authors acknowledged the anonymous reviewers for comments to improve the quality of this work.

Funding Open access funding provided by The Ministry of Higher Education Malaysia and Universiti Putra Malaysia. Universiti Putra Malaysia, GP-IPM/9750400, Alvin Lim Teik Zheng.

Declarations

Conflict of interest The authors declare that they have no known competing financial interests or personal relationships that could have appeared to influence the work reported in this paper.

Consent for Publication All authors reviewed and agreed to the final manuscript for publication.

Open Access This article is licensed under a Creative Commons Attribution 4.0 International License, which permits use, sharing, adaptation, distribution and reproduction in any medium or format, as long as you give appropriate credit to the original author(s) and the source, provide a link to the Creative Commons licence, and indicate if changes were made. The images or other third party material in this article are included in the article's Creative Commons licence, unless indicated otherwise in a credit line to the material. If material is not included in the article's Creative Commons licence and your intended use is not permitted by statutory regulation or exceeds the permitted use, you will need to obtain permission directly from the copyright holder. To view a copy of this licence, visit <http://creativecommons.org/licenses/by/4.0/>.

References

- Zulkifli, S.N.; Rahim, H.A.; Lau, W.-J.: Detection of contaminants in water supply: a review on state-of-the-art monitoring technologies and their applications. *Sens. Actuators B Chem.* **255**, 2657–2689 (2018). <https://doi.org/10.1016/j.snb.2017.09.078>
- Zheng, A.L.T.; Teo, E.Y.L.; Yiu, P.H.; Boonyuen, S.; Chung, E.L.T.; Andou, Y.: Recent advances in ultrasensitive electrochemical sensors and biosensors for determination of antibiotics in environment samples. *Clean Technol. Environ. Policy* (2024). <https://doi.org/10.1007/s10098-024-02934-8>
- Zheng, A.L.T.; Teo, E.Y.L.; Seenivasagam, S.; Yiu, P.H.; Boonyuen, S.; Chung, E.L.T.; Andou, Y.: Recent review on porous adsorbents for water decontamination: strategies for enhanced removal of tetracycline. *J. Porous Mater.* (2024). <https://doi.org/10.1007/s10934-024-01699-1>
- Zheng, A.L.T.; Teo, E.Y.L.; Seenivasagam, S.; Yiu, P.H.; Boonyuen, S.; Chung, E.L.T.; Lease, J.; Andou, Y.: Nanostructures embedded on porous materials for the catalytic reduction of nitrophenols: a concise review. *J. Porous Mater.* **31**, 1557–1575 (2024). <https://doi.org/10.1007/s10934-024-01618-4>
- Ortúzar, M.; Esterhuizen, M.; Olicón-Hernández, D.R.; González-López, J.; Aranda, E.: Pharmaceutical pollution in aquatic environments: a concise review of environmental impacts and bioremediation systems. *Front. Microbiol.* (2022). <https://doi.org/10.3389/fmicb.2022.869332>
- Li, X.; Shen, X.; Jiang, W.; Xi, Y.; Li, S.: Comprehensive review of emerging contaminants: detection technologies, environmental impact, and management strategies. *Ecotoxicol. Environ. Saf.* **278**, 116420 (2024). <https://doi.org/10.1016/j.ecoenv.2024.116420>
- Kumar, R.; Qureshi, M.; Vishwakarma, D.K.; Al-Ansari, N.; Kuriqi, A.; Elbeltagi, A.; Saraswat, A.: A review on emerging water contaminants and the application of sustainable removal technologies. *Case Stud. Chem. Environ. Eng.* **6**, 100219 (2022). <https://doi.org/10.1016/j.csee.2022.100219>
- Chang, D.; Mao, Y.; Qiu, W.; Wu, Y.; Cai, B.: The source and distribution of tetracycline antibiotics in China: a review. *Toxics* **11**, 214 (2023). <https://doi.org/10.3390/toxics11030214>
- Amangelsin, Y.; Semenova, Y.; Dadar, M.; Aljofan, M.; Björklund, G.: The impact of tetracycline pollution on the aquatic environment and removal strategies. *Antibiotics* **12**, 440 (2023). <https://doi.org/10.3390/antibiotics12030440>
- Nasrollahi, N.; Vatanpour, V.; Khataee, A.: Removal of antibiotics from wastewaters by membrane technology: limitations, successes, and future improvements. *Sci. Total. Environ.* **838**, 156010 (2022). <https://doi.org/10.1016/j.scitotenv.2022.156010>
- Zheng, A.L.T.; Ohno, T.; Andou, Y.: Recent progress in photocatalytic efficiency of hybrid three-dimensional (3D) graphene architectures for pollution remediation. *Top. Catal.* **65**, 1634–1647 (2022). <https://doi.org/10.1007/s11244-022-01610-9>
- Zheng, A.L.T.; Andou, Y.: Hybrid three-dimensional (3D) graphene architectures for photocatalysis of noxious pollutants. In: *Green Nanoarchitectonics*, pp. 47–72. Jenny Stanford Publishing, New York (2022)
- Zheng, A.L.T.; Boonyuen, S.; Andou, Y.: Porous Graphene-Based Materials for Enhanced Adsorption Towards Emerging Micropollutants (EMs). Presented at the (2023)
- Zheng, A.L.T.; Che Abdullah, C.A.; Andou, Y.: Graphene-based nanomaterials for water remediation applications. In: *Handbook of Green and Sustainable Nanotechnology*, pp. 1097–1122. Springer International Publishing, Cham (2023)
- Jeffrey, K.B.; Zheng, A.L.T.; Hii, T.T.; Seng, K.W.K.; Chung, E.L.T.; Lease, J.; Andou, Y.: Sustainable dye wastewater treatment: utilizing duckweed-derived adsorbents for efficient methylene blue removal. *Biomass Convers. Biorefin.* (2024). <https://doi.org/10.1007/s13399-024-06432-1>
- Kumari, H.; Sonia; Suman; Ranga, R.; Chahal, S.; Devi, S.; Sharma, S.; Kumar, S.; Kumar, P.; Kumar, S.; Kumar, A.; Parmar, R.: A review on photocatalysis used for wastewater treatment: dye degradation. *Water Air Soil Pollut. Pollut.* (2023). <https://doi.org/10.1007/s11270-023-06359-9>
- Premalatha, N.; Rex, P.: A comprehensive review on photocatalytic degradation of organophosphorus pesticide using ZnO coupled photocatalysts. *Desalin. Water Treat.* **320**, 100753 (2024). <https://doi.org/10.1016/j.dwt.2024.100753>
- Zheng, A.L.T.; Sabidi, S.; Ohno, T.; Maeda, T.; Andou, Y.: Cu₂O/TiO₂ decorated on cellulose nanofiber/reduced graphene hydrogel for enhanced photocatalytic activity and its antibacterial applications. *Chemosphere* **286**, 131731 (2022). <https://doi.org/10.1016/j.chemosphere.2021.131731>
- Shanmugam, P.; Parasuraman, B.; Boonyuen, S.; Thangavelu, P.; AlSalhi, M.S.; Zheng, A.L.T.; Viji, A.: Hydrothermal synthesis and photocatalytic application of ZnS-Ag composites based on biomass-derived carbon aerogel for the visible light degradation of methylene blue. *Environ. Geochem. Health* **46**, 92 (2024). <https://doi.org/10.1007/s10653-024-01871-1>
- Lau, G.E.; Che Abdullah, C.A.; Wan Ahmad, W.A.N.; Assaw, S.; Zheng, A.L.T.: Eco-friendly photocatalysts for degradation of dyes. *Catalysts* **10**, 1129 (2020). <https://doi.org/10.3390/catal10101129>
- Kamble, G.S.; Natarajan, T.S.; Patil, S.S.; Thomas, M.; Chougale, R.K.; Sanadi, P.D.; Siddharth, U.S.; Ling, Y.-C.: BiVO₄ As a



- sustainable and emerging photocatalyst: synthesis methodologies, engineering properties, and its volatile organic compounds degradation efficiency. *Nanomaterials* **13**, 1528 (2023). <https://doi.org/10.3390/nano13091528>
22. Kalidasan, K.; Mallapur, S.; Munirathnam, K.; Nagarajaiah, H.; Reddy, M.B.M.; Kakarla, R.R.; Raghu, A.V.: Transition metals-doped g-C₃N₄ nanostructures as advanced photocatalysts for energy and environmental applications. *Chemosphere* **352**, 141354 (2024). <https://doi.org/10.1016/j.chemosphere.2024.141354>
 23. Mohtar, S.S.; Aziz, F.; Ismail, A.F.; Sambudi, N.S.; Abdullah, H.; Rosli, A.N.; Ohtani, B.: Impact of doping and additive applications on photocatalyst textural properties in removing organic pollutants: a review. *Catalysts* **11**, 1160 (2021). <https://doi.org/10.3390/catal11101160>
 24. Sultana, M.; Mondal, A.; Islam, S.; Khatun, M.A.; Rahaman, M.H.; Chakraborty, A.K.; Rahman, M.S.; Rahman, M.M.; Nur, A.S.M.: Strategic development of metal doped TiO₂ photocatalysts for enhanced dye degradation activity under UV-Vis irradiation: a review. *Curr. Res. Green Sustain. Chem.* **7**, 100383 (2023). <https://doi.org/10.1016/j.crgsc.2023.100383>
 25. Zheng, A.L.T.; Sinin, A.E.; Jin, W.T.; Feng, K.L.; Boonyuen, S.; Chung, E.L.T.; Lease, J.; Andou, Y.: Rare earth elements for enhancing photocatalysis in pollutant degradation and water treatment. *Int. J. Environ. Sci. Technol.* (2024). <https://doi.org/10.1007/s13762-024-06203-5>
 26. Afriyie, C.; Zhang, X.: New Fe-doped two-dimensional BiVO₄ nanosheets for direct methane conversion to methyl oxygenates. *Mater Adv.* **5**, 3981–3991 (2024). <https://doi.org/10.1039/D4MA00069B>
 27. Thakur, S.; Ojha, A.; Kansal, S.K.; Gupta, N.K.; Swart, H.C.; Cho, J.; Kuznetsov, A.; Sun, S.; Prakash, J.: Advances in powder nano-photocatalysts as pollutant removal and as emerging contaminants in water: analysis of pros and cons on health and environment. *Adv. Powder Mater.* **3**, 100233 (2024). <https://doi.org/10.1016/j.apmate.2024.100233>
 28. Regmi, C.; Kshetri, Y.K.; Kim, T.-H.; Pandey, R.P.; Lee, S.W.: Visible-light-induced Fe-doped BiVO₄ photocatalyst for contaminated water treatment. *Mol. Catal.* **432**, 220–231 (2017). <https://doi.org/10.1016/j.mcat.2017.02.004>
 29. Hemavibool, K.; Sansanya, T.; Nanan, S.: Enhanced photocatalytic degradation of tetracycline and oxytetracycline antibiotics by BiVO₄ photocatalyst under visible light and solar light irradiation. *Antibiotics* **11**, 761 (2022). <https://doi.org/10.3390/antibiotics11060761>
 30. Mansha, M.S.; Iqbal, T.; Farooq, M.; Riaz, K.N.; Afsheen, S.; Sultan, M.S.; Al-Zaqri, N.; Warad, I.; Masood, A.: Facile hydrothermal synthesis of BiVO₄ nanomaterials for degradation of industrial waste. *Heliyon* **9**, e15978 (2023). <https://doi.org/10.1016/j.heliyon.2023.e15978>
 31. Din, I.U.; Saeed, T.; Ahmad, Z.; Naeem, A.; Alharthi, A.I.; Alotaibi, M.A.: A comparative study for the effect of calcination on the temperature-dependant magnetic properties of cobalt ferrite nanoparticles. *J. Superhard Mater. Superhard Mater.* **43**, 278–284 (2021). <https://doi.org/10.3103/S106345762104002X>
 32. Abrishami-Rad, A.; Sadeghzadeh-Attar, A.: Fe-doped BiVO₄ photocatalyst assisting SnO₂ nanorod arrays for efficient visible-light-driven degradation of Basic Red 46. *J. Taiwan Inst. Chem. Eng.* **151**, 105110 (2023). <https://doi.org/10.1016/j.jtice.2023.105110>
 33. Chaiwichian, S.; Wetchakun, K.; Phanichphant, S.; Kangwansupamonkon, W.; Wetchakun, N.: The effect of iron doping on the photocatalytic activity of a Bi₂WO₆-BiVO₄ composite. *RSC Adv.* **6**, 54060–54068 (2016). <https://doi.org/10.1039/C6RA07811G>
 34. Liu, R.; Ren, J.; Zhao, D.; Ning, J.; Zhang, Z.; Wang, Y.; Zhong, Y.; Zheng, C.; Hu, Y.: Band-gap engineering of porous BiVO₄ nanoshuttles by Fe and Mo co-doping for efficient photocatalytic water oxidation. *Inorg. Chem. Front.* **4**, 2045–2054 (2017). <https://doi.org/10.1039/C7QI00588A>
 35. Wu, G.-R.; Sun, L.-J.; Xu, J.-K.; Gao, S.-Q.; Tan, X.-S.; Lin, Y.-W.: Efficient degradation of tetracycline antibiotics by engineered myoglobin with high peroxidase activity. *Molecules* **27**, 8660 (2022). <https://doi.org/10.3390/molecules27248660>
 36. Guo, M.; Jin, Z.; Pan, J.; Xu, J.; Guo, L.; Yin, X.-B.; Lu, N.; Zhang, M.: Construction of COFs@MoS₂-Pd hierarchical tubular heterostructures for enhanced catalytic performance. *Inorg. Chem.* **63**, 18263–18275 (2024). <https://doi.org/10.1021/acs.inorgchem.4c03151>
 37. Zhuang, Q.; Li, X.; Lian, X.; Hu, H.; Wang, N.; Wu, J.; Miao, K.; Feng, G.; Luo, X.: Catalysis enhancement of Co₃O₄ through the epitaxial growth of inert ZnO in peroxymonosulfate activation: the catalytic mechanism of surface hydroxyls in singlet oxygen generation. *Cryst. Growth Des.* **25**, 319–329 (2025). <https://doi.org/10.1021/acs.cgd.4c01357>
 38. Shan, Z.; Yang, Y.; Shi, H.; Zhu, J.; Tan, X.; Luan, Y.; Jiang, Z.; Wang, P.; Qin, J.: Hollow dodecahedra graphene oxide-cuprous oxide nanocomposites with effective photocatalytic and bactericidal activity. *Front. Chem.* (2021). <https://doi.org/10.3389/fchem.2021.755836>
 39. Wang, N.; Zhang, Z.; Zhang, Y.; Xu, X.; Guan, Q.: Fe-Mn oxide activating persulfate for the in-situ chemical remediation of organic contaminated groundwater. *Sep. Purif. Technol. Purif. Technol.* **355**, 129566 (2025). <https://doi.org/10.1016/j.seppur.2024.129566>
 40. Gu, W.; Lu, D.; Kondamareddy, K.K.; Li, J.; Cheng, P.; Ho, W.; Wang, Y.; Zhao, Z.; Wang, Z.: Efficient photocatalytic decomposition of NO and mechanism insight enabled by NaBH₄-reduced N(ligancy-3)-vacancy-rich-graphitic carbon nitride. *Mater. Today Phys.* **46**, 101487 (2024). <https://doi.org/10.1016/j.mtphys.2024.101487>
 41. Dai, F.; Zhuang, Q.; Huang, G.; Deng, H.; Zhang, X.: Infrared spectrum characteristics and quantification of OH groups in coal. *ACS Omega* **8**, 17064–17076 (2023). <https://doi.org/10.1021/acsomega.3c01336>
 42. Rychtowski, P.; Tryba, B.; Skrzypaska, A.; Felczak, P.; Sreńscek-Nazzal, J.; Wróbel, R.J.; Nishiguchi, H.; Toyoda, M.: Role of the hydroxyl groups coordinated to TiO₂ surface on the photocatalytic decomposition of ethylene at different ambient conditions. *Catalysts* **12**, 386 (2022). <https://doi.org/10.3390/catal12040386>
 43. Wechprasit, T.; Bootchanont, A.; Sailuam, W.; Wattanawikkam, C.; Kansaard, T.; Noinonmueng, T.; Mekprasart, W.; Chirawatkul, P.; Jayasankar, C.K.; Pecharapa, W.; Boonyarattanakalin, K.: Structural and photocatalytic properties and X-ray absorption spectroscopic study of BiVO₄ nanoparticles incorporated with Fe synthesized by sonochemical method. *Radiat. Phys. Chem. Phys. Chem.* **201**, 110480 (2022). <https://doi.org/10.1016/j.radphyschem.2022.110480>
 44. Zhang, L.; Chen, D.; Jiao, X.: Monoclinic structured BiVO₄ nanosheets: hydrothermal preparation, formation mechanism, and coloristic and photocatalytic properties. *J. Phys. Chem. B* **110**, 2668–2673 (2006). <https://doi.org/10.1021/jp056367d>
 45. Mammeri, O.; Bouremmad, F.; Chouikh, F.; Benamira, M.; Akika, F.Z.; Can, M.M.; Avramova, I.; Djermoune, A.: Pure monoclinic n-BiVO₄ prepared by modified sol-gel method for high efficiency photodegradation of methylene blue under solar light irradiation. *React. Kinetics Mech. Catal.* (2024). <https://doi.org/10.1007/s11144-024-02765-0>
 46. Silambarasan, M.; Saravanan, S.; Soga, T.: Effect of Fe-doping on the structural, morphological and optical properties of ZnO nanoparticles synthesized by solution combustion process. *Phys. E Low Dimens. Syst. Nanostruct.* **71**, 109–116 (2015). <https://doi.org/10.1016/j.physe.2015.04.002>
 47. Pardeshi, S.K.; Patil, A.B.: Effect of morphology and crystallite size on solar photocatalytic activity of zinc oxide synthesized by



- solution free mechanochemical method. *J. Mol. Catal. A Chem.* **308**, 32–40 (2009). <https://doi.org/10.1016/j.molcata.2009.03.023>
48. Wang, X.; Sø, L.; Su, R.; Wendt, S.; Hald, P.; Mamakhel, A.; Yang, C.; Huang, Y.; Iversen, B.B.; Besenbacher, F.: The influence of crystallite size and crystallinity of anatase nanoparticles on the photo-degradation of phenol. *J. Catal. Catal.* **310**, 100–108 (2014). <https://doi.org/10.1016/j.jcat.2013.04.022>
 49. Zafar, Z.; Yi, S.; Li, J.; Li, C.; Zhu, Y.; Zada, A.; Yao, W.; Liu, Z.; Yue, X.: Recent development in defects engineered photocatalysts: an overview of the experimental and theoretical strategies. *Energy Environ. Mater.* **5**, 68–114 (2022). <https://doi.org/10.1002/eem2.12171>
 50. Xu, F.; He, Y.; Zhang, J.; Liang, G.; Liu, C.; Yu, J.: Prolonging charge carrier lifetime via intraband defect levels in s-scheme heterojunctions for artificial photosynthesis. *Angew. Chem. Int. Ed. Chem. Int. Ed.* (2024). <https://doi.org/10.1002/anie.202414672>
 51. Dey, K.K.; Gahlawat, S.; Ingole, P.P.: BiVO₄ optimized to nano-worm morphology for enhanced activity towards photoelectrochemical water splitting. *J. Mater. Chem. A Mater.* **7**, 21207–21221 (2019). <https://doi.org/10.1039/C9TA07353A>
 52. Velmurugan, S.; Jothi, K.J.; Pakrudheen, I.; Nagarani, S.; Mubarak, S.; Devanesan, S.; AlSalhi, M.S.: Template-free synthesis of the highly ordered, efficient nano Nd₂O₃-TiO₂ for visible-light-driven photocatalytic degradation of rhodamine B. *Ceram. Int.* (2024). <https://doi.org/10.1016/j.ceramint.2024.12.107>
 53. Fan, X.; Liang, H.; Song, Y.; Xing, Z.; Bai, J.: Development of a novel beads-like In/Fe co-doped BiVO₄ composite for enhanced photocatalytic degradation of tetracycline in water. *Colloids Surf A Physicochem Eng Asp Physicochem. Eng. Asp.* **687**, 133477 (2024). <https://doi.org/10.1016/j.colsurfa.2024.133477>
 54. Hasham Firooz, M.; Naderi, A.; Moradi, M.; Kalantary, R.R.: Enhanced tetracycline degradation with TiO₂/natural pyrite S-scheme photocatalyst. *Sci. Rep.* **14**, 4954 (2024). <https://doi.org/10.1038/s41598-024-54549-0>
 55. Liaqat, M.; Younas, A.; Iqbal, T.; Afsheen, S.; Zubair, M.; Kamran, S.K.S.; Syed, A.; Bahkali, A.H.; Wong, L.S.: Synthesis and characterization of ZnO/BiVO₄ nanocomposites as heterogeneous photocatalysts for antimicrobial activities and waste water treatment. *Mater. Chem. Phys.* **315**, 128923 (2024). <https://doi.org/10.1016/j.matchemphys.2024.128923>
 56. Murzin, D.Yu.: On surface heterogeneity and catalytic kinetics. *Ind. Eng. Chem. Res.* **44**, 1688–1697 (2005). <https://doi.org/10.1021/ie049044x>
 57. Serpone, N.: Some remarks on so-called heterogeneous photocatalysis and on the mechanical application of the Langmuir-Hinshelwood kinetic model. *J. Adv. Oxid. Technol.* (2007). <https://doi.org/10.1515/jaots-2007-0119>
 58. Hassaan, M.A.; El-Nemr, M.A.; Elkatory, M.R.; Ragab, S.; Niculescu, V.-C.; El Nemr, A.: Principles of photocatalysts and their different applications: a review. *Top. Curr. Chem. Curr. Chem.* **381**, 31 (2023). <https://doi.org/10.1007/s41061-023-00444-7>
 59. Cai, Y.; Fan, J.; Liu, Z.: Enhanced degradation of tetracycline over FeS-based Fenton-like process: autocatalytic decomposition of H₂O₂ and reduction of Fe(III). *J. Hazard. Mater.* **436**, 129092 (2022). <https://doi.org/10.1016/j.jhazmat.2022.129092>
 60. Cui, J.-Y.; Li, T.-T.; Chen, L.; Wang, J.-J.: Advancing BiVO₄ photoanode activity for ethylene glycol oxidation via strategic pH control. *Molecules* **29**, 2783 (2024). <https://doi.org/10.3390/molecules29122783>
 61. Nguyen, T.D.; Nguyen, V.-H.; Nanda, S.; Vo, D.-V.N.; Nguyen, V.H.; Van Tran, T.; Nong, L.X.; Nguyen, T.T.; Bach, L.-G.; Abdullah, B.; Hong, S.-S.; Van Nguyen, T.: BiVO₄ photocatalysis design and applications to oxygen production and degradation of organic compounds: a review. *Environ. Chem. Lett.* **18**, 1779–1801 (2020). <https://doi.org/10.1007/s10311-020-01039-0>
 62. Yan, B.; Li, X.; Wang, X.; Yang, P.; Lu, H.; Zhang, X.: Degradation efficiency and mechanism of tetracycline in water by activated persulfate using biochar-loaded nano zero-valent iron. *Molecules* **29**, 3875 (2024). <https://doi.org/10.3390/molecules29163875>
 63. Wannakan, K.; Khansamrit, K.; Senasu, T.; Nanan, S.: Ultrasound-assisted synthesis of a ZnO/BiVO₄ S-scheme heterojunction photocatalyst for degradation of the reactive red 141 dye and oxytetracycline antibiotic. *ACS Omega* **8**, 4835–4852 (2023). <https://doi.org/10.1021/acsomega.2c07020>
 64. Katz, A.; McDonagh, A.; Tijjing, L.; Shon, H.K.: Fouling and inactivation of titanium dioxide-based photocatalytic systems. *Crit. Rev. Environ. Sci. Technol.* **45**, 1880–1915 (2015). <https://doi.org/10.1080/10643389.2014.1000763>
 65. Soni, V.; Singh, P.; Khan, A.A.P.; Singh, A.; Nadda, A.K.; Husain, C.M.; Van Le, Q.; Rizevsky, S.; Nguyen, V.-H.; Raizada, P.: Photocatalytic transition-metal-oxides-based p-n heterojunction materials: synthesis, sustainable energy and environmental applications, and perspectives. *J. Nanostruct. Chem.* **13**, 129–166 (2023). <https://doi.org/10.1007/s40097-021-00462-1>
 66. Yang, J.; Deng, C.; Lei, Y.; Duan, M.; Yang, Y.; Chen, X.; Yang, S.; Li, J.; Sheng, H.; Shi, W.; Chen, C.; Zhao, J.: Fe–N Co-doped BiVO₄ photoanode with record photocurrent for water oxidation. *Angew. Chem. Chem.* (2025). <https://doi.org/10.1002/ange.202416340>
 67. Wang, Y.; Huang, J.; Chen, Y.; Yang, H.; Ye, K.-H.; Huang, Y.: Modulating built-in electric field via Bi-VO₄-Fe interfacial bridges to enhance charge separation for efficient photoelectrochemical water splitting. *J. Colloid Interface Sci.* **672**, 12–20 (2024). <https://doi.org/10.1016/j.jcis.2024.05.218>
 68. Gaffar, S.; Kumar, A.; Alam, J.; Riaz, U.: Efficient visible light-induced photocatalytic degradation of tetracycline hydrochloride using CuFe₂O₄ and PANI/CuFe₂O₄ nanohybrids. *Environ. Sci. Pollut. Res. Pollut. Res.* **30**, 108878–108888 (2023). <https://doi.org/10.1007/s11356-023-29976-7>
 69. Serrà, A.; Gómez, E.; Michler, J.; Philippe, L.: Facile cost-effective fabrication of Cu@Cu₂O@CuO-microalgae photocatalyst with enhanced visible light degradation of tetracycline. *Chem. Eng. J.* **413**, 127477 (2021). <https://doi.org/10.1016/j.cej.2020.127477>
 70. Senasu, T.; Youngme, S.; Hemavibool, K.; Nanan, S.: Sunlight-driven photodegradation of oxytetracycline antibiotic by BiVO₄ photocatalyst. *J. Solid State Chem.* **297**, 122088 (2021). <https://doi.org/10.1016/j.jssc.2021.122088>
 71. Xia, C.; Ou, X.; Chen, P.; Zhang, F.; Wei, M.; Wang, Y.; Zhang, M.: Sunlight degradation of tetracycline by Z-type BiOI/g-C₃N₄ photocatalyst synthesized via a simple two-step process: response surface methods, degradation pathways, toxicity evaluation. *J. Water Process Eng.* **64**, 105617 (2024). <https://doi.org/10.1016/j.jwpe.2024.105617>
 72. Pei, Z.; Guo, H.; Zhu, L.; Li, C.; Fu, Z.; Xu, J.: Photocatalytic degradation of various antibiotics under visible light irradiation by CdS-doped SiO₂@BiOX (X = Br, Cl) prepared by mixed solvothermal method. *Mater. Sci. Eng. B* **287**, 116134 (2023). <https://doi.org/10.1016/j.mseb.2022.116134>
 73. Maggu, C.; Singla, S.; Basu, S.: Unleashing the power of sunlight: Bi₂O₃/Sb₂S₃ photocatalysis for sustainable wastewater remediation of tetracycline and rhodamine-B. *J. Environ. Manag.* **349**, 119424 (2024). <https://doi.org/10.1016/j.jenvman.2023.119424>
 74. Kumar, G.; Dutta, R.K.: Fabrication of plate-on-plate SnS₂/Bi₂WO₆ nanocomposite as photocatalyst for sunlight mediated degradation of antibiotics in aqueous medium. *J. Phys. Chem. Solids* **164**, 110639 (2022). <https://doi.org/10.1016/j.jpics.2022.110639>
 75. Wang, X.; Wang, X.; Zhang, H.; Zhang, J.; Li, Z.; Wang, X.; Xu, J.; Cao, D.; Li, J.; Lu, C.: Photothermal-assisted photocatalytic degradation of tetracycline in simulated natural water by BiVO₄/CuBi₂O₄ Z-scheme heterojunction: mechanisms insight,

- degradation pathways and toxicity assessment. *Process. Saf. Environ. Prot. Saf. Environ. Prot.* **188**, 1292–1305 (2024). <https://doi.org/10.1016/j.psep.2024.06.042>
76. Gao, X.; Xiao, F.; Yang, C.; Wang, J.; Su, X.: Hydrothermal fabrication of W18O49 nanowire networks with superior performance for water treatment. *J Mater Chem A Mater.* **1**, 5831 (2013). <https://doi.org/10.1039/c3ta10724h>
77. Zheng, A.L.T.; Boonyuen, S.; Ohno, T.; Andou, Y.: Hydrothermally reduced graphene hydrogel intercalated with divalent ions for dye adsorption studies. *Processes* **9**, 169 (2021). <https://doi.org/10.3390/pr9010169>
78. Gomathi, A.; Priyadharsan, A.; Prabhuraj, T.; Vasanthi, G.; Gokilapriya, S.; Ramesh Kumar, K.A.; Maadeswaran, P.: Boosting the performance of solar light driven CeO2/BiVO4 anchored g-C3N4 nanocomposites: a systematic study toward the development of a photocatalytic and antibacterial activity. *Colloids Surf A Physicochem Eng Asp Physicochem. Eng. Asp.* **673**, 131835 (2023). <https://doi.org/10.1016/j.colsurfa.2023.131835>
79. Brade, H.; Opal, S.M.; Vogel, S.N.; Morrison, D.C. (eds.): *Endotoxin in health and disease*. CRC Press, Berlin (2020)
80. Wan Osman, W.N.A.; Rosli, M.H.; Mazli, W.N.A.; Samsuri, S.: Comparative review of biodiesel production and purification. *Carbon Capture Sci. Technol.* **13**, 100264 (2024). <https://doi.org/10.1016/j.ccst.2024.100264>

Authors and Affiliations

Melissa Alexander Maran¹ · Alvin Lim Teik Zheng^{1,2}  · Hui Yan Tan³ · Shahrul Razid Sarbini³ · Kar Ban Tan⁴ · Supakorn Boonyuen⁵ · Kelly Kai Seng Wong⁶ · Eric Lim Teik Chung^{7,8} · Jacqueline Lease⁹ · Yoshito Andou^{9,10}

✉ Alvin Lim Teik Zheng
alvintz@upm.edu.my

Melissa Alexander Maran
s32852@student.upm.edu.my

Hui Yan Tan
gs63839@student.upm.edu.my

Shahrul Razid Sarbini
shahrulrazid@upm.edu.my

Kar Ban Tan
tankarban@upm.edu.my

Supakorn Boonyuen
supakorn@tu.ac.th

Kelly Kai Seng Wong
kellywong@upm.edu.my

Eric Lim Teik Chung
ericlim@upm.edu.my

Jacqueline Lease
lease.jacqueline708@mail.kyutech.jp

Yoshito Andou
yando@life.kyutech.ac.jp

- ¹ Department of Science and Technology, Faculty of Humanities, Management and Science, Universiti Putra Malaysia Bintulu Campus, 97008 Bintulu, Sarawak, Malaysia
- ² Institute of Ecoscience Borneo, Universiti Putra Malaysia Bintulu Campus, 97008 Bintulu, Sarawak, Malaysia
- ³ Department of Crop Science, Faculty of Agricultural Science and Forestry, Universiti Putra Malaysia Kampus Bintulu Sarawak, 97008 Bintulu, Sarawak, Malaysia
- ⁴ Department of Chemistry, Faculty of Science, Universiti Putra Malaysia, 43400 Serdang, Selangor, Malaysia
- ⁵ Department of Chemistry, Faculty of Science and Technology, Thammasat University, Pathumthani 12120, Thailand
- ⁶ Department of Agribusiness and Bioresource Economics, Faculty of Agriculture, Universiti Putra Malaysia, 43400 Serdang, Malaysia
- ⁷ Department of Animal Science, Faculty of Agriculture, Universiti Putra Malaysia, 43400 Serdang, Malaysia
- ⁸ Institute of Tropical Agriculture and Food Security, Universiti Putra Malaysia, 43400 Serdang, Malaysia
- ⁹ Graduate School of Life Sciences and Systems Engineering, Kyushu Institute of Technology, Fukuoka 808-0196, Japan
- ¹⁰ Collaborative Research Centre for Green Materials on Environmental Technology, Kyushu Institute of Technology, Fukuoka 808-0196, Japan

